npj | quantum materials

Review

Published in partnership with Nanjing University

https://doi.org/10.1038/s41535-026-00877-5

Surveying optically addressable spin qubits for quantum information and sensing technology

Check for updates

Calysta A. Tesiman, Mark Oxborrow ✉ & Max Attwood ✉

Quantum technologies offer ways to solve certain tasks more quickly, efficiently, and with greater precision than their classical counterparts. Yet substantial challenges remain in the construction of sufficiently error-free and scalable quantum platforms needed to unlock any real benefits to society. Acknowledging that this hardware can take vastly different forms, our review here focuses on materials that bear an optically-addressable electron or nuclear spin to embody qubits. Towards helping the reader to spot trends and pick winners, we have surveyed the various families of optically addressable spin qubits and attempted to benchmark and identify the most promising ones in each. We go on to reveal further trends that demonstrate how qubit lifetimes depend on the material's synthesis, the concentration/distribution of its embedded qubits, and the experimental conditions.

Over the last 40 years, quantum computation has progressed from concept to hardware. In 2023, IBM reported the commissioning of a 1121-qubit superconducting quantum processor[1], while Honeywell demonstrated a quantum charge-coupled device architecture based on trapped ions[2]. Despite such achievements, the scalability and, thus, ultimate utility of each species of hardware remains contested.

Recently, materials that harbour an unpaired electronic or nuclear spin have garnered attention as contenders for use as qubit media. The best of these materials offer coherence times exceeding milliseconds, albeit at cryogenic temperatures[3]. Progress in the field has made the dream of usefully storing quantum information and/or implementing quantum processing at scale with appropriately interacting spins more tangible. For example, the start-up company Quantum Brilliance recently demonstrated a room temperature qubit system based on nitrogen-vacancy (NV) centres in diamond[4]. Beyond computation, these same materials are already providing advantageous forms of quantum sensing, especially under ambient conditions where thermally-driven electronic and photonic noise present significant challenges for quantum applications[5]. Their advantages stem from the ability to optically initialise spin states into highly non-Boltzmann populations and, likewise, to implement optical readout routines that are less impacted by blackbody radiation.

In these quantum spin materials, information is most simply encoded in the spin state of a two-level system, but can be encoded across multiple levels in high-spin ($S \geq 1$) systems; a property that may be used to facilitate certain error correction protocols[6]. For qubits, a magnetic or electric field is applied to split otherwise degenerate spin states. The higher and lower energy spin states, $|0\rangle$ and $|1\rangle$, form two orthogonal basis states. A pure state is formed as a coherent superposition of the two ($|\psi\rangle = a|0\rangle + b|1\rangle$, see Fig. 1a). Geometrically, we can visualise any such state as a point on the surface of a Bloch sphere, the location being defined by a polar angle θ and an azimuthal angle ϕ[7]. The value of θ determines the probability amplitude of finding the qubit in either the $|0\rangle$ or $|1\rangle$ state, while ϕ determines the relative phase of the qubit between the $|0\rangle$ and $|1\rangle$ states.pdf.

To be useful, these materials must enable both reliable spin addressability and long storage times. These properties are, in turn, limited by the materials' spin-lattice relaxation (T_1) and spin decoherence times (T_2, also known as phase memory time). T_1 and T_2 represent the time it takes for the "longitudinal" and "transverse" magnitude of the spin-state vector, respectively, to decay by a factor of e (Fig. 1a, c). In practical terms, T_1 is the lifetime of a non-Boltzmann spin population (Fig. 1b), and, put simply by DiVincenzo[8,9], T_2 characterises the interactions of a spin qubit with its environment. These quantities are fundamentally related by $1/T_2 = 1/2T_1 + 1/T_\phi$, where $1/T_\phi$ stems from contributions of so-called "pure dephasing" due to factors such as 1/f noise[10], spin-bath fluctuations, and other magnetic/electric field gradients. Hence, in an idealised "Markovian" system, T_2 is only the decoherence time constant due to energy exchange with the environment (with the limit $1/T_2 = 1/2T_1$)[11], and can be estimated by the homogeneous linewidth of a spin transition's resonant frequency ($\Delta_{hom} = 1/\pi T_2$, Fig. 1d). In most cases, T_ϕ is significant and the transition linewidth becomes inhomogeneously broadened and can be used to estimate the overall spin dephasing, $1/T_2^* = 1/T_2 + 1/T_\phi = \Delta_{inhom}/\pi$, Fig. 1e)[12]. Sources of spin dephasing can arise from both intra- and intermolecular interactions, and T_2 is limited by several controllable

Department of Materials and London Centre for Nanotechnology, Imperial College London, London, UK. ✉e-mail: m.oxborrow@imperial.ac.uk; m.attwood@imperial.ac.uk

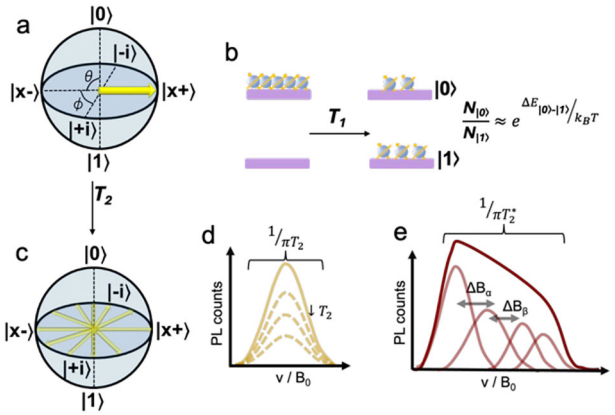


Fig. 1 | Quantum spin parameters important for quantum technology. a Bloch sphere representation of a spin vector showing a quantum state composed of $|\psi\rangle = (|0\rangle + |1\rangle)/\sqrt{2}$. **b** Spin-lattice relaxation T_1 transforms an ensemble of polarised spins to a Boltzmann (thermal) spin distribution, approximated by the equation shown, where $N_{|0\rangle/|1\rangle}$ is the population of each state, $\Delta E_{|0\rangle-|1\rangle}$ is the energy difference between each state, k_B is the Boltzmann constant, and T is temperature. **c** Bloch sphere representing an incoherent collective superposition for an ensemble of spins after time T_2 has elapsed. **d** Homogeneous spin-resonance linewidth, demonstrating the impact of lowering T_2, and **e** the inhomogeneous linewidth broadened by neighbouring (α and β) magnetic spins; ν and B_0 represent the microwave frequency and magnetic field, respectively, as commonly used independent variables in quantum sensing.

factors in the material's spin state, spin-orbit coupling (SOC), phonons, spin concentration, and spatial distribution of nuclear and electronic spins[13]. Spin-relaxation parameters are most commonly measured using electron paramagnetic resonance (EPR) techniques by measuring microwave absorptions and emissions from a material as a function of frequency or magnetic field strength, forming the basis for quantum spin technologies (Fig. 2).

Quantum systems capable of operating at room temperature open up many additional applications that the overhead of cryogenic operation precludes. But, achieving high fidelity (in the initialisation, gate operations and readout) of room temperature qubits remains extremely challenging. In this review, we have attempted to survey the available "fully-optically-addressable materials" (FOAMs) that are most directly relevant to quantum information and sensing technology[14]. We do not provide an exhaustive account of all reported spin systems and their limitations. Rather, we present the different approaches, materials-wise, that have shown promise and report the properties (where available) of the best-performing representatives of each approach.

Overview of candidate spin-qubit materials

FOAMs are an attractive option for quantum applications since they typically involve spin levels that are energetically separated by far more than k_BT and can be initialised using visible/near-infrared light to generate quasi-"pure" quantum states. Furthermore, optical signals, composed of photons with energies far larger than k_BT, are less affected by thermal noise and benefit from the availability of single-photon sources and detectors capable of operating at high levels of fidelity even at room temperature. FOAMS are

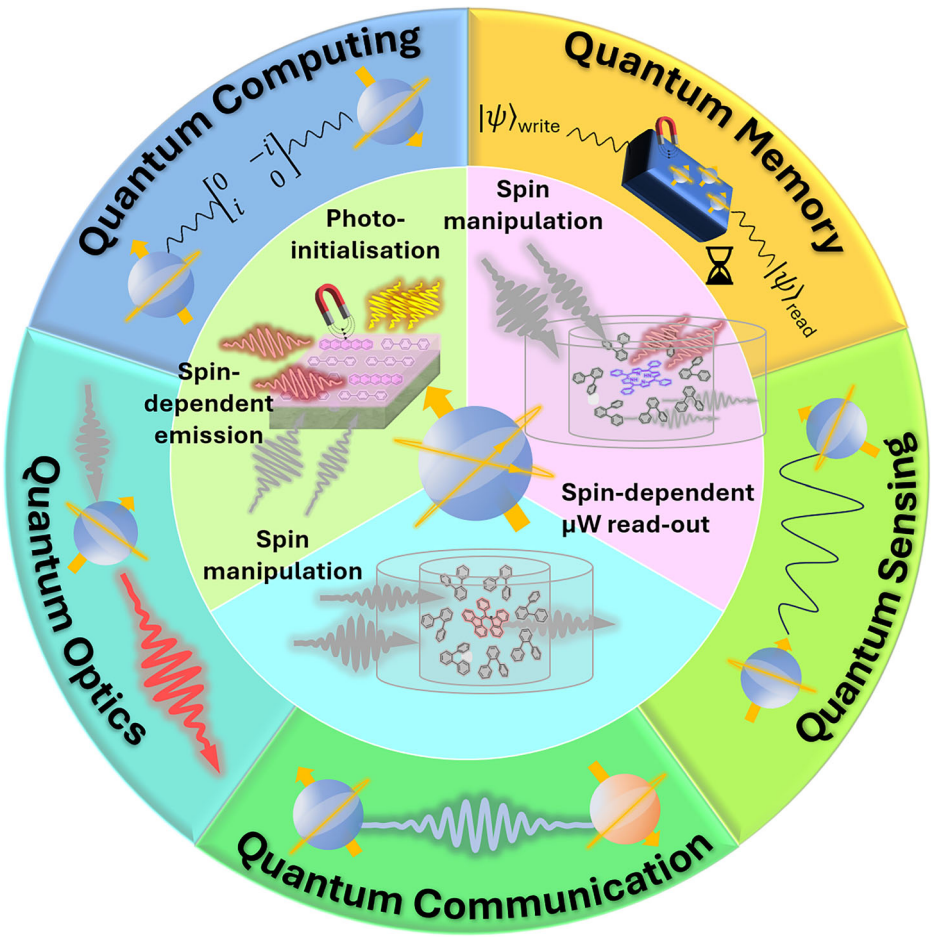


Fig. 2 | Prominent approaches for addressing quantum spins for quantum applications (inner circle) and their applications in quantum technologies (outer circle). Optically-detected magnetic resonance (ODMR) spin measurements utilise spin-dependent luminescence with light/microwave-based spin manipulation (green third), whilst electron paramagnetic resonance (EPR) spin measurements can employ light to initialise a spin system into a spin-polarised state (pink third) or one can employ microwaves to manipulate a thermally polarised system with spin-dependent microwave readout (blue third).

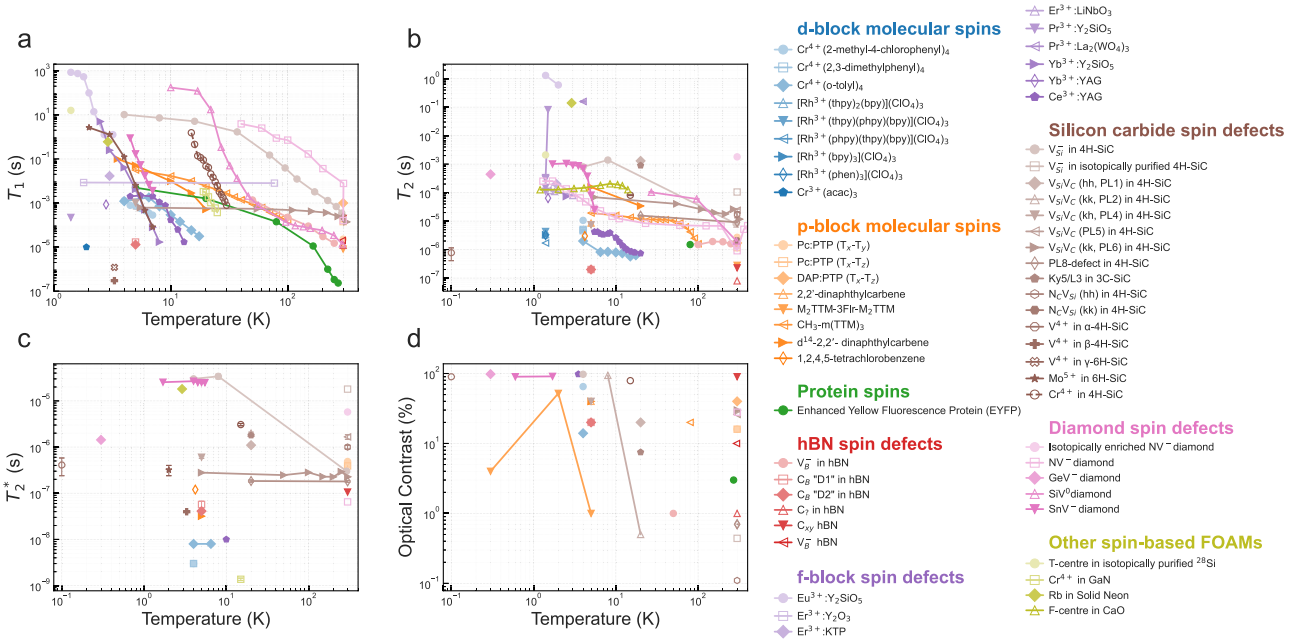


Fig. 3 | A collection of reported temperature-dependent quantum spin parameters measured using pulsed-ODMR techniques. a Spin-lattice relaxation, **b** spin coherence, **c** spin dephasing times, and **d** optical contrast. Not every parameter has been reported for each system and condition, hence not every material will be visible on all four plots. In each case, we have opted to include the highest measured parameter using standard inversion/saturation recovery, 3-pulse echo and Ramsey technique, regardless of applied magnetic field. Data adapted from: 0.1% Pc:PTP[121,123], M_2TTM-3FIr-M_2TTM[135], CH_3-m(TTM)$_2$[136], 2,2′-dinaphthylcarbene[193], 1,2,4,5-tetrachlorobenzene[112], Cr^{4+} molecular systems[111,151]; Rh^{3+} molecular systems[147], NV-diamond[24,194,195], isotopically enriched NV-diamond[25], SiV^-diamond[45,196] SnV^-diamond[47], GeV^-diamond[46]; V_B^- in hBN[92], carbon defects in hBN[96,98,101], monovacancies in 4H-SiC[57,67], isotopically purified SiC[68], divacancies in 4H-SiC[69,73,74,197–199], N_C V_{Si} (hh) in 4H-SiC[58], N_C V_{Si} (kk) in 4H-SiC[59], Cr^{4+} in 4H-SiC[60], Mo^{5+} in 6H-SiC[64], V^{4+} in 4/6H-SiC[79], Cr^{4+} in GaN[60], Eu^{3+} in Y_2O_3[173], Er^{3+} in Y_2O_3[178,200], Y_2SiO_5[3], KTP[179], and $LiNbO_4$[178,201]; Pr^{3+} in Y_2SiO_5[167] and $La_2(WO_4)_3$[177]; Yb^{3+} in Y_2SiO_5[181] and YAG[180]; Ce^{3+}:YAG[187,202]. Rb in solid Ne[203], T-centre in ^{28}Si[204], EYFP protein[143], F-centre in CaO[205].

often probed using ODMR spectroscopy, where the quantum sensing sensitivity for a.c. magnetic fields (for example), η, is proportional to $\sqrt{t_{\mathrm{overhead}}}/(C\sqrt{n_{\mathrm{spin}}n_{\mathrm{avgs}}}T_2^*)$, where t_{overhead} is the duration of the readout process, C is the measurement contrast, n_{spin} is the number of spins, and n_{avgs} is the number of scan averages. Relatively few FOAMs have been demonstrated so far and are often limited by either low photoluminescence yields or relatively short-lived spin polarisations (T_1) and spin coherences (T_2), which have been summarised in Fig. 3 to support our discussion. As a prerequisite for inclusion in Fig. 3, we have opted to follow the criteria put forward by Weber et al.[15], for the realisation of an optically addressable solid-state spin qubit (that is usable)

1. A state must be paramagnetic and support two or more energy levels,
2. An optical pumping cycle can be used to initialise the qubit,
3. Luminescence to or from the qubit state varies by qubit sub-level in some differentiable way (i.e. intensity, wavelength, or other properties),
4. Optical transitions must not interfere with the electronic state of the host,
5. Differences between qubit sublevels must be large enough to avoid thermal excitation.

3D spin-defect FOAMs

Diamond spin centres. A well-established example of a FOAM which satisfies the above criteria is the negatively charged NY centres in diamond (herein simply, NV-diamond or NV^--centres), which utilise a triplet ground state and the hyperfine splitting arising from the $I = 1$ ^{14}N-nucleus. Initialisation (i.e., electron spin polarisation) is achieved by optical excitation with green light. The newly generated excited states either relax by emission of 637 nm light or undergo intersystem crossing (ISC) into a metastable singlet state (Fig. 4a). Repopulation of the ground state then follows an intermediate relaxation between two singlet states (with emission at 1042 nm) and finally spin-selective ISC into the T_0 sub-level, resulting in a strong spin polarisation. At zero-applied magnetic field (ZF), the $T_{\pm1}$ states are degenerate due to the defect's C_{3v} symmetry. The application of a magnetic field lifts this degeneracy, which enables spin manipulation using microwave pulses, thereby modifying the fluorescence at characteristic Zeeman splitting frequencies ($h\nu = g_e\mu_B B_0$), which can be detected following subsequent optical excitations and fluorescence back to T_0.

NV-diamond has been a cornerstone of ODMR-based quantum sensing due to its robust spin properties even at room temperature. Due to the relatively low spin densities (resulting in small dipolar coupling between spins) and the mismatch between diamond lattice vibrations (phonons) and the Larmor frequency of electron spins, its $S = 1$ ground state, NV-diamond can exhibit T_1s of several milliseconds at room temperature[16,17]. The nature and mechanism of its spin-lattice relaxation as a function of temperature, which includes an "Orbach-like" process (dependent on the phonon density at the spin-transition frequency) and spin-phonon Raman scattering (of either first[18] or else second[17] order) scaling like T^5, have been repeatedly investigated.

The material's quantum spin properties are highly dependent on the NV^--centres's depth (below the diamond's surface)[19], concentration[20], crystal strain[21], and the presence of impurities such as ^{13}C, N-centres or EPR-inactive neutral or positively charged NV-centres[22,23]. Its popularity has seen a plethora of investigations to understand and modulate its spin properties. For example, high-field EPR spectroscopy and temperature-dependent measurements have demonstrated that decoherence from the ^{14}N and ^{13}C flip-flop fluctuations can be almost eliminated at low temperatures where the spin bath is polarised[24]. Here, T_2 reached ≈ 250 μs at 2 K, following a sharp increase below 12 K in high-temperature high-pressure diamond samples. Achieving similar properties under low-field and higher temperature conditions with thermally polarised nuclei is challenging and requires meticulous materials preparation and/or the use of dynamical decoupling methods. For example, the impact of parasitic nuclear spins and

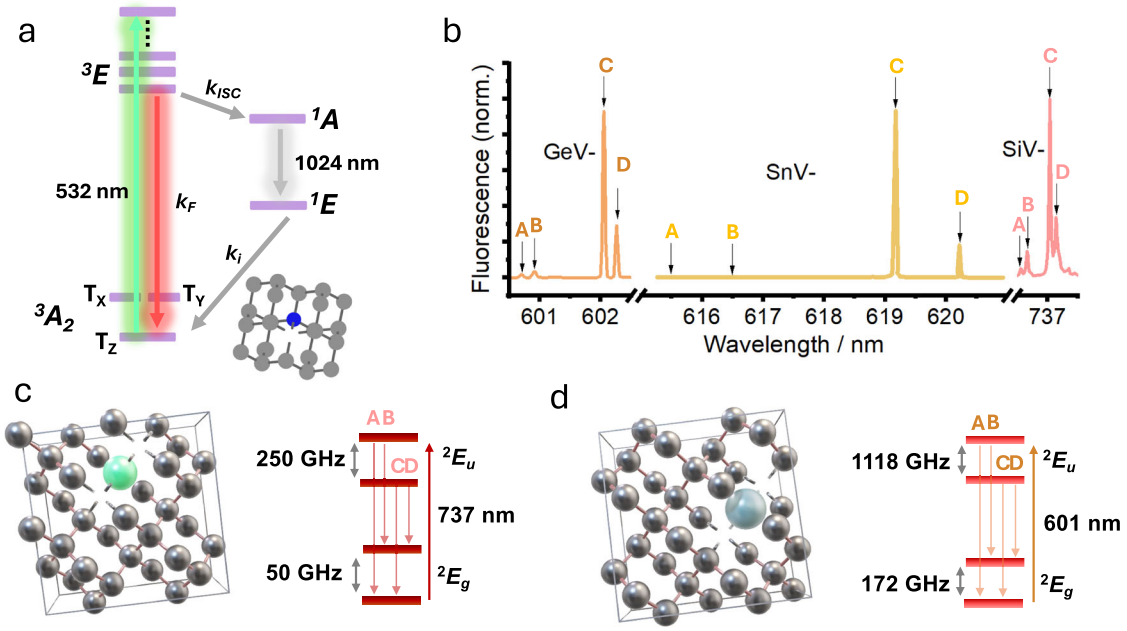


Fig. 4 | Selected spin defects in diamond. a Jablonski diagram for NV-diamond as a prototypical example of an optically addressable material; **b** low-temperature fluorescence spectrum for SiV^-, SnV^- and GeV^- singlet spin centres showing electronic transitions between electronic and spin-orbit energy levels used for optically addressing spins; **c** example defect structure and energy level diagram for SiV^- and **d** GeV^- spin centres. Fluorescence data adapted from refs. 36,48,206.

impurities was shown most remarkably by Balasuramanian et al.[25]. Careful growth by chemical vapour deposition (CVD) on a diamond substrate using isotopically enriched feedstock led to just 0.3% ^{13}C abundance and low levels of other paramagnetic impurities, resulting in $T_2 \approx 1.8$ ms at room temperature.

One limitation of NV^--centres in diamond is their propensity to undergo charge-state conversion into a neutral and magnetically inactive state, NV^0, during high laser power excitation. This spin-independent process is reversible, but results in an EPR-inactive parasitic reservoir of NV^0 that results in the loss of spin polarisation by up to 31% during pulsed measurements[26] and can even out-compete T_1 relaxometry[27].

More recently, increasing attention has been paid to using diamonds as a host for other spin defects owing to diamond's wide bandgap, efficient thermal dissipation, and physical and chemical stability. As such, various magnetically-active colour centres have been investigated for quantum applications[28]. These include HV[29], BV[30], OV[31], so-called group-IV vacancy defects[32] such as SiV[33,34], SnV[35,36], GeV[37], and PbV[38,39], and even transition metal defects originating as impurities like NiV[40]. To our knowledge, spin polarisation has not been observed in HV or OV centres, whilst ODMR experiments on BV and PbV have not been reported. Despite this, PbV in particular, both in charged PbV^- and neutral PbV^0 states, is expected to exhibit robust spin coherence properties up to 9 K[41].

Metal-vacancy spin-centres typically exhibit strong spin-orbit coupling (several hundred GHz) that gives rise to zero-field splitting (ZFS) even for $S = 1/2$ species, as well as electron-nuclear spin coupling, making them qudit candidates (Fig. 4b–d). Moreover, group-IV defects exhibit useful photonic properties that make them attractive for quantum applications such as Fourier-limited zero-phonon line (ZPL) linewidths, high spectral stability, coherent photon emission, and strain-responsive bandgap engineering[42].

For example, negatively charged SiV ($S = 1/2$ system, Fig. 4c) has enabled direct observation of photon interference[43]. Outside of a dilution refrigerator, the spin coherence lifetimes are severely impacted by thermal acoustic phonon coupling. At 100 mK, T_1 reaches 1 second while the longest T_2^* measured was 1.5 µs. Spin coherence could be maintained by dynamical decoupling up to 600 mK where the coherence time during a dynamical decoupling scheme (T_{DD}) measured 60 µs. T_2^* can also be improved through strain engineering, which modifies the spin-orbit coupling and is responsible for inducing the ground-state splitting, and subsequently the spin-phonon coupling[44]. By comparison, the neutral SiV ($S = 1$ ground state) demonstrates an impressive $T_1 \approx 25$ s, $T_2 \approx 0.1$ ms, even at 15 K, decreasing to 7.8 and 2 µs at room temperature[45]. However, a route to reliably synthesising SiVs in diamonds remains elusive.

Negatively charged GeV ($S = 1/2$ ground state, Fig. 4d) has been investigated using ODMR for quantum memory applications at 300 mK and found to exhibit a $T_2 \approx 440$ µs and $T_2^* \approx 1.46$ µs[46]. These defects were found to be particularly responsive to dynamical decoupling protocols with T_{DD} reaching 24 ms, representing a significant improvement compared to negatively charged SiV.

SnV^-s ($S = 1/2$ ground state) are also robust spin centres and have been the subject of spin control experiments. Rosenthal et al. report $T_1 \approx 20$ ms and $T_2 \approx 170$ µs when measured at 1.7 K in highly strained SnV-centres; these spin lifetimes afford significant improvement in operation fidelity[47]. By comparison, Trusheim et al. report a longer $T_1 \approx 1.26$ ms and $T_2^* \approx 540$ ns at 2.9 K in a less strained system[48].

Negatively charged NiV-centres ($S = 1/2$) are near-infrared emitters, making them especially interesting for quantum communications due to their compatibility with conventional optical cables[28]. The $S = 1/2$ ground state of the negatively charged NiV-centre has a predicted 0.1 ms coherence time at 4 K[49], but only recently have steady-state ODMR studies been reported[40].

Silicon carbide spin centres. Beyond diamond, silicon carbide (SiC) also shows promising optical and coherence properties for quantum applications[50–55]. SiC is a complex material with >200 polymorphs. It is also used commercially in electronics and hence benefits from decades of manufacturing maturation. So far, the study of quantum systems has been largely restricted to 3C-, 4H-, and 6H-SiC, where C and H signify cubic and hexagonal structures, respectively, and the preceding number designates its polytype[56] (see Fig. 5a). Pure SiC has a wide bandgap (≈2–3 eV), weak spin-orbit coupling, and a naturally low abundance of nuclear spins. Importantly, it is capable of harbouring several varieties of optically addressable colour centre with (often) near-infrared emission

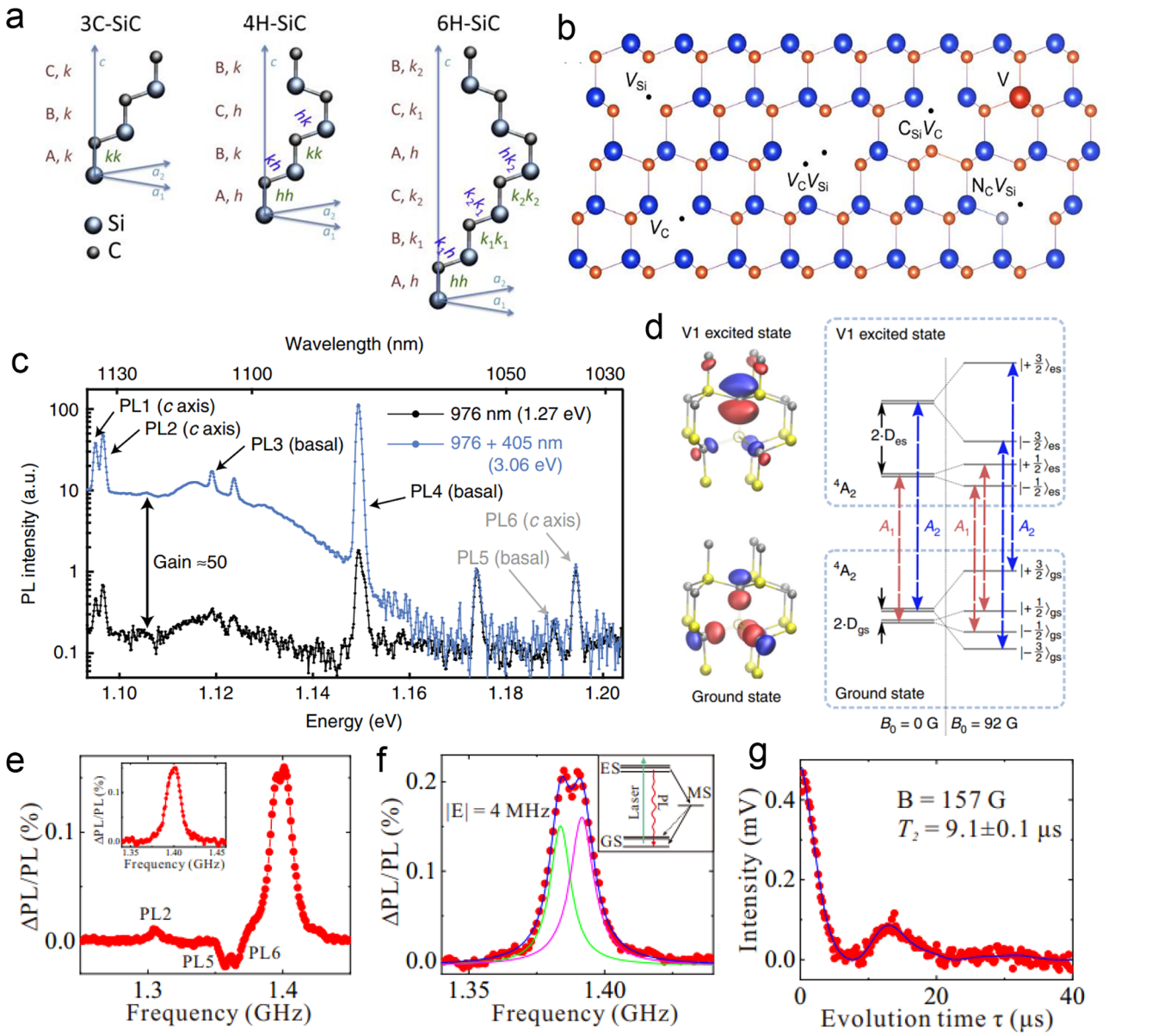


Fig. 5 | Optically addressable point defects in SiC. a Structures of the most commonly studied SiC polytypes, 3C-SiH, 4H-SiC and 6H-SiC showing the origin of divancancy nomenclature depending on the lattice substitution site; **b** 2D-depiction of selected SiC ODMR-active defects. **c** Photoluminescence spectrum from a SiC ensemble showing multiple individually addressable defect types (PL1-PL6). **d** Orbital distribution for the ground and excited states of the V_B^--defect with the corresponding quartet spin-level energy diagram with and without an applied magnetic field. Red and blue arrows indicate optical transitions that connect $m_s = |1/2\rangle$ and $m_s = |3/2\rangle$ states, respectively. **e** ODMR spectrum of 4H-SiC samples at 20 K and **f** 300 K (inset optical initialisation scheme), demonstrating the robust spin-optical properties of the PL8-defect (the highest contrast peak), **g** the corresponding room temperature Hahn-echo decay trace for PL8. Figure 1**a**–**e**–**g** were reproduced from refs. 57,74,207–209, respectively, with permission from MDPI and the American Chemical Society under the open access Creative Commons licence.

and record ODMR contrasts[57]. The most commonly studied defects encompass monovacancies (V_C or V_{Si}), and divacancies, but other defects may include carbon antisite vacancies ($C_{Si}V_C$) (see Fig. 5b), charged NVs[58,59], Cr^{4+}-[60,61], V^{3+}, V^{4+}[62,63], Mo^{5+}[64], and Ti-centres[55,56,65]. Further layers of complexity are added by consideration of additional charge states and crystallographic sites within each polytype. Understandably, studies often focus on the "best-performing" defect within a given sample, and seldom are single samples of SiC homogeneous. This lack of homogeneity is perhaps the material's most significant practical limitation as a spin-qubit candidate compared to other platforms.

Nevertheless, several defects exhibit outstanding spin-optical properties, and the fabrication challenges are beginning to be addressed. Negatively charged V_{Si} in isotopically purified (^{28}Si) 4H-SiC exhibits the largest ODMR contrast at ≈97% at 4 K[57]. With an $S = 3/2$ ground state, its associated ZFS is a few MHz with degenerate pairs of $|1/2\rangle$ and $|3/2\rangle$ states (Fig. 5d). Under a magnetic field (≈82 mT) precisely aligned to the crystallographic c-axis, this degeneracy is lost, and in the excited, so-called "V1" state, $|3/2\rangle$ shifts higher in energy than the $|1/2\rangle$ states. To achieve ≈97% contrast, the authors first equilibrate the spin populations using a 40 μs off-resonance pump (at 730 nm), followed by an on-resonance pump (at 861 nm) lasting up to 80 μs. On-resonance optical pumping causes $|3/2\rangle$ states to selectively decay into a non-radiative metastable state, followed by spin-selective repopulation of $|1/2\rangle$ ground states. This leads to a spin polarisation of up to 90%, which is paired with record T_2s and T_2^* s of 0.8 ± 0.12 ms and 30 ± 2 μs, respectively.

At room temperature, dynamic decoupling techniques can be used to extend T_2 from 8 μs to 47 ± 20 ms[66]. More recently, it was shown that V_{Si} defects can be implanted into nanophotonic waveguides fabricated from

4H-SiC while also controlling the alignment of individual defects and maintaining excellent spin-optical properties[67]. Here, T_2^* of bulk V_{Si}-centres was measured at 34 ± 4 µs at 10 K, whilst those in the ≈1 µm diameter waveguides were measured at 9.4 ± 0.7 µs. The coherence properties can be further improved by a factor of 10 through a regime of isotopic purification, and another factor of 5 by reducing strain inhomogeneity through a regime of annealing. Using this combined approach, Lekavicius et al. enhanced T_2^* from 400 ns to ≈20 µs at room temperature[68].

Divacancies also exhibit compelling spin-optical properties, including up to 94% optical contrast[69], albeit at generally lower temperatures. Divacancies are formed by annealing pre-irradiated SiC at over 700 °C, however, the conversion efficiency into divacancies only ever reaches a few percent[70,71], which may in part be due to counterproductive divacancy-dissociation back into V_C, V_{Si}, and potentially even antisite-C_{Si} V_C-centres under the right conditions[72]. Divacancies are most often given the generic label "V_{Si} V_C", designating that these neutral defects occur when both a carbon and a silicon atom are missing from the lattice. However, it is important to note that depending on the polytype, there are several crystallographic sites available (Fig. 5a, b), and it is even possible to generate defects within stacking faults. Therefore, V_{Si} V_C-defects can exhibit either c-axis, C_{3v}, or basal-type, C_{1h}, symmetry. As a result, in 4H-SiC alone, there are at least eight unique divacancies, the best known examples of which are sometimes colloquially called PL1-8, and are all distinguishable by their unique ZPL emission frequency (Fig. 5c) and are mostly assigned to have $S = 1$ ground state due to their circa 1 GHz ZFS (Fig. 5e).

The kk-divacancy, PL2 in 4H-SiC, with natural isotopic abundance, can demonstrate T_2s of 1.3 ms at 20 K when decoupled from ^{13}C and ^{29}Si nuclear spins under a 30 mT field[73]; which is significantly longer than NV-diamond under similar conditions. Moreover, NV^--centres in 4H-SiC (N_C V_{Si}) have known kk, hh, hk and kh-type defects and also exhibit robust spin parameters at room temperature[58,59]. However, unlike their diamond analogue, N_C V_{Si}s benefit from an NIR-emission with four distinct ZPLs between 1170 and 1250 nm, which is a preferred region for biosensing applications. Some of these divacancy centres also demonstrate remarkable insensitivity to temperature. For example, Yan et al. reported that despite having an unknown structure, PL8-centres exhibit similarly intense ODMR signatures at 1.4 GHz when measured at 20 K or room temperature[74] (Fig. 5e, f). This temperature insensitivity is also reflected in the quantum spin properties where T_2 and T_2^* measure 15.6 ± 0.5 µs and 184 ± 10 ns at 20 K, respectively, and 9.1 ± 0.1 µs and 180 ± 9 ns at room temperature, respectively (Fig. 5g). This long-lived room temperature spin coherence is shared to a lesser extent by PL6-centres, which are thought to be hh-divacancies occupying a stacking fault and are distinguishable by their 1038 nm (vs PL8's 1007 nm) ZPL emission. This demonstrates that several species in SiC are suitable for room temperature quantum applications. Moreover, divacancy systems were the first spin-centres demonstrated to be amenable to all-electrical spin-ensemble readout and initialisation schemes[75,76]. These functionalities have since been discovered with monovacancies under ambient conditions[77], demonstrating a strong potential to avoid some of the difficulties associated with ODMR spectroscopy, such as pump-light stability and photon collection efficiency.

Beyond vacancy systems, several metal-ion centres have demonstrated interesting spin-optical properties when implanted into SiC. The best to date in terms of its optical addressability is Cr^{4+} in 4H-SiC. As an $S = 1$ species, this material exhibits $T_1 > 1$ second, with T_2 and $T_2^* = 81$ µs and 317 ns, respectively, at 15 K[61]. Importantly, it also demonstrates a 79% contrast, marking it as a system with one of the highest optical readout fidelities. The spin-optical properties of the same ion are markedly impaired in GaN host, which demonstrates 27× broader emission linewidths due to interactions of Cr^{4+}-centres with the surrounding spin bath[60].

V^{4+} is perhaps the most thoroughly studied ion with coherent manipulation of its $S = 1/2$ spin system reported in α-4H-SiC[78], β-4H-SiC, and γ-6H-SiC[79] host matrices. Whilst generally the spin-relaxation parameters are shorter than Cr^{4+}, all V^{4+} defects emit ~1.3 µm with markedly narrow inhomogeneous emission linewidth (ca. 100 MHz) and resolvable hyperfine coupling of the electron spin to the $I = 7/2$ ^{51}V nucleus, making them promising candidates for low-loss o-telecom band quantum applications[80]. Unlike most of the spin-defects discussed so far, spin polarisation of V^{4+} is achieved using a magnetic field to lift the zero-field degeneracy of the $m_s \pm 1/2$ states to generate two distinct spin-dependent ZPLs which can be selectively depopulated using circularly polarised light[81]. This scheme has been used successfully to generate strong ensemble spin polarisation, resulting in reported pulsed-ODMR contrasts of up to 90%[82]. Care is needed, however, since use of an on-resonance (with the ZPL) initialisation scheme generates V^{3+} states, which can be compensated for using an off-resonance green or UV repump protocol.

Mo^{5+} defects in 6H-SiC are another $S = 1/2$ spin defect demonstrated to enable coherent spin manipulation at cryogenic temperatures. Here, rather than being a hindrance, the strong SOC of the heavy Mo^{5+}-ion is thought to protect it from parasitic phonon modes and spin-spin interactions, leading to T_1 of 2.7 seconds at 2 K[64], significantly longer than V^{4+}. However, its ZPL is broader than vanadium at 24 GHz at 4 K, and shifted to 1120 nm[83], which is slightly outside the highly desirable telecom band.

2D- and van der Waals FOAMs

Van der Waals (vdW) materials are made of 2D-atomically thin layers weakly bound together through van der Waals interactions. These include graphene, hexagonal boron nitride (hBN) and transition metal dichalcogenides. Despite a range of remarkable materials having been identified as ODMR-active, the precise structure and even spin multiplicity of the spin species are often ambiguous. Nevertheless, like other defect spin-qubit systems, inhomogeneous broadening and spin-phonon interactions are the principal causes of spin decoherence.

The prototypical vdW material, graphene, was an early candidate for harbouring spin qubits; however, the metallic band structure of graphene is not conducive to forming luminescent spin centres. Instead, its isoelectronic analogue, hBN, has been the centre of remarkable advancement as a 2D-optically addressable platform at room temperature, building off its success as a single-photon source[84]. Magnetically-active spin centres in hBN were identified by EPR in the 1960s, with hyperfine structures giving clues to their identity as $S = 1/2$ boron centres and carbon impurities[85–87]. However, the first optically addressable spin centres were only identified recently as triplets stemming from a negatively charged vacancy, likely originating from a missing boron atom, so-called V_B^--centres[88–91] (Fig. 6a). Similar to NV-diamond, optical initialisation is achieved by photoexcitation with 532 nm light, leading to ISC into a metastable singlet, which spin-selectively repopulates the fluorescent $m_s = 0$ state (T_Z at ZF, Fig. 6b). The readout of the spin state occurs through 850 nm fluorescence with pulsed-ODMR contrast of ≈1% at room temperature and almost ≈30% at 10 K, revealing a ZFS of $|D|$ ≈ 3.5 GHz (Fig. 6c). Spin-relaxation and Hahn-echo measurements reveal a room temperature T_1 of 18 µs and T_2 of 2 µs[92]. These properties are particularly remarkable since both boron and nitrogen exhibit isotopically abundant nuclear spins (^{14}N, $I = 1$, ^{10}B, $I = 3$, and ^{11}B, $I = 3/2$). In the same work, suppression of the nuclear spin bath using a second microwave source centred on a hyperfine line was found to improve T_1 and T_2 up to 25 µs and 7.5 µs, respectively. Work continues optimising the synthesis conditions for hBN to enhance the quantum properties of the defects. For instance, the contrast of V_B^--centres can be increased to ≈10% at room temperature by controlling the material purity and electron irradiation dose, though T_1 appears to remain phonon limited[93].

Due to hBN's potential as a tunable single-photon source, significant effort has been made to control substitutional-defect structures through careful synthesis. CVD-grown hBN has been found to contain a plethora of optically active carbon and oxygen-based spin species with stable ZFLs in the visible range[94,95]; although most have yet to be structurally characterised, or even the multiplicity conclusively determined (see Fig. 6d for candidate structures and Fig. 6e for the spin initialisation scheme). For example, three distinct so-called "C_B"-defects, likely stemming from the substitution of a boron or nitrogen atom by carbon ("D1", "D2", "D3", all likely $S = 1/2$), demonstrate similar spin relaxation and coherence quantum properties (T_2

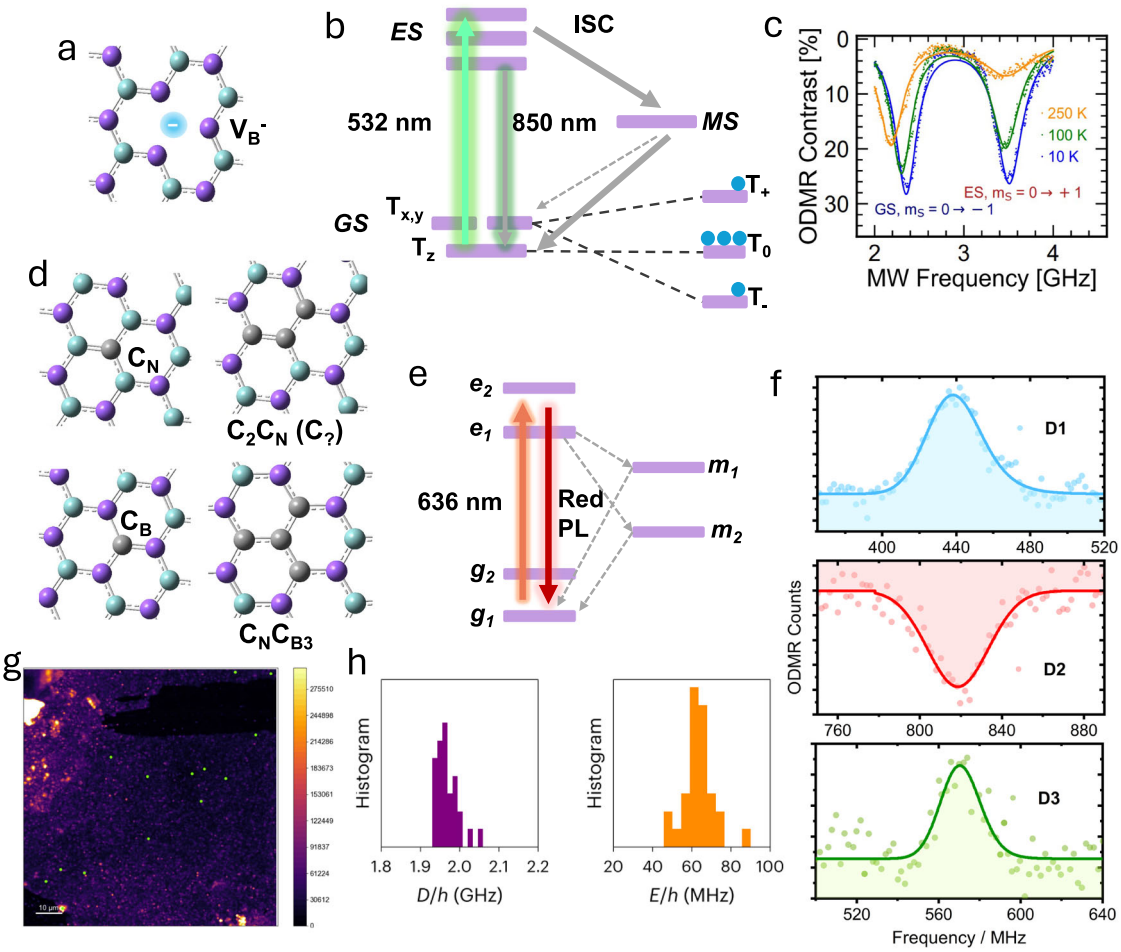


Fig. 6 | Optically addressable spin defects in hBN. a Proposed structure for the V_B^- triplet spin centre (purple atoms = N, cyan atoms = boron and grey atoms = carbon, with **b** its corresponding Jablonski diagram, and **c** variable temperature ODMR spectra at low-field, confirming the defect's triplet character. **d** Proposed structures for selected carbon-based defects in hBN with **e** Jablonski diagram showing the involvement of two metastable states and repopulation of the g_1-state to achieve spin initialisation. **f** ODMR spectra for three carbon defects measured at 5 K showing $g \approx 2$ doublet resonances corresponding to 154, 290, and 200 G for D1, D2, and D3-defects, respectively. **g** 2D-confocal map of hBN flakes showing fluorescent and ODMR-active (green dots) defect sites, with **h** histograms for 400+ carbon-based triplet defects. **c**, (**f**, data only), **g**, **h** were adapted from refs. 90,96,98, respectively, with permission from Springer Nature under the open access Creative Commons licence.

≈ 0.2 μs) with a continuous-wave (CW)-optical contrast up to 20% at 5 K[96] (Fig. 6f). Their inhomogeneous linewidths are also limited by the nuclear spin bath ($T_2^* \approx 40$–60 ns), where local spins also bestow an apparent ZFS of between 8-10 MHz.

Though ensemble measurements remain challenging due to carbon-doped hBN's broad emission profile, a recent report has shown that it is possible to survey over 400 defect centres in CVD-grown samples. Collectively known as "C_{xy}"-centres, careful measurements of individual spin-centres reveal distinctive triplet character with a ZFS of 15 MHz in contrast to most other accepted carbon-defects found in hBN[97]. The triplet identity was later unambiguously characterised and confirmed for a series of defects with significantly larger ZFS with $|D| \approx 2$ GHz and $|E| \approx 50 - 80$ MHz[98] (Fig. 6g, h). The T_1 at room temperature was measured to be 200 ± 30 μs, $T_2 \approx 1$ μs and $T_2^* \approx 100$ ns, competitive with V_B^- defects. However, these properties are matched with a remarkable ODMR contrast of almost 50% (though it decreases with an applied magnetic field), giving rise to projected D.C. magnetic field sensitivity of up to 3 μT $Hz^{-1/2}$. A recent survey of similar defects demonstrated that under high microwave and optical pump powers, the optical contrast could reach as high as 90%, though most exhibit < 50% despite similar ZFS, T_1 and T_2[99]. The authors explore the potential of this material as a medium for D.C. vectorial quantum magnetometry by taking advantage of the defects' low symmetry and in-plane quantisation axis. Though not yet experimentally verified, the authors hypothesise that applying a field bias along a different material axis corresponding to each of the three triplet states, T_x, T_y, and T_z, should result in subtle changes in contrast that can be related to particular T_n states to yield 3-vector components of the applied field.

More complex carbon species demonstrating similar coherent behaviour at room temperature have been explored using metal-organic vapour-phase epitaxy with carbon-based additives[100,101]. The so-called "$C_?$"-defect (potential identity C_2C_N) is another potential $S = 1/2$ species or, two weakly coupled $S = 1/2$ centres, has recently been reported as being co-located with V_B^--centres following electron irradiation of hBN flakes[101]. While their T_1 and T_2 are similar to C_B-species (≈13 μs and ≈80 ns, respectively), it can be used to "sense" V_B^--centres through spin cross relaxation at an appropriate applied magnetic field. Due to its out-of-plane magnetic quantisation axis (versus the in-plane axis of V_B^--centres), it can also be used more effectively to image magnetic structure on underlying substrates with an estimated DC magnetic sensitivity of ≈1 μT $Hz^{-1/2}$.

One limitation of hBN spin defects is their propensity to form dark "trap" states that lead to blinking luminescence[102,103]. Unlike NV-diamond, the formation of these dark trap states is not dependent on laser

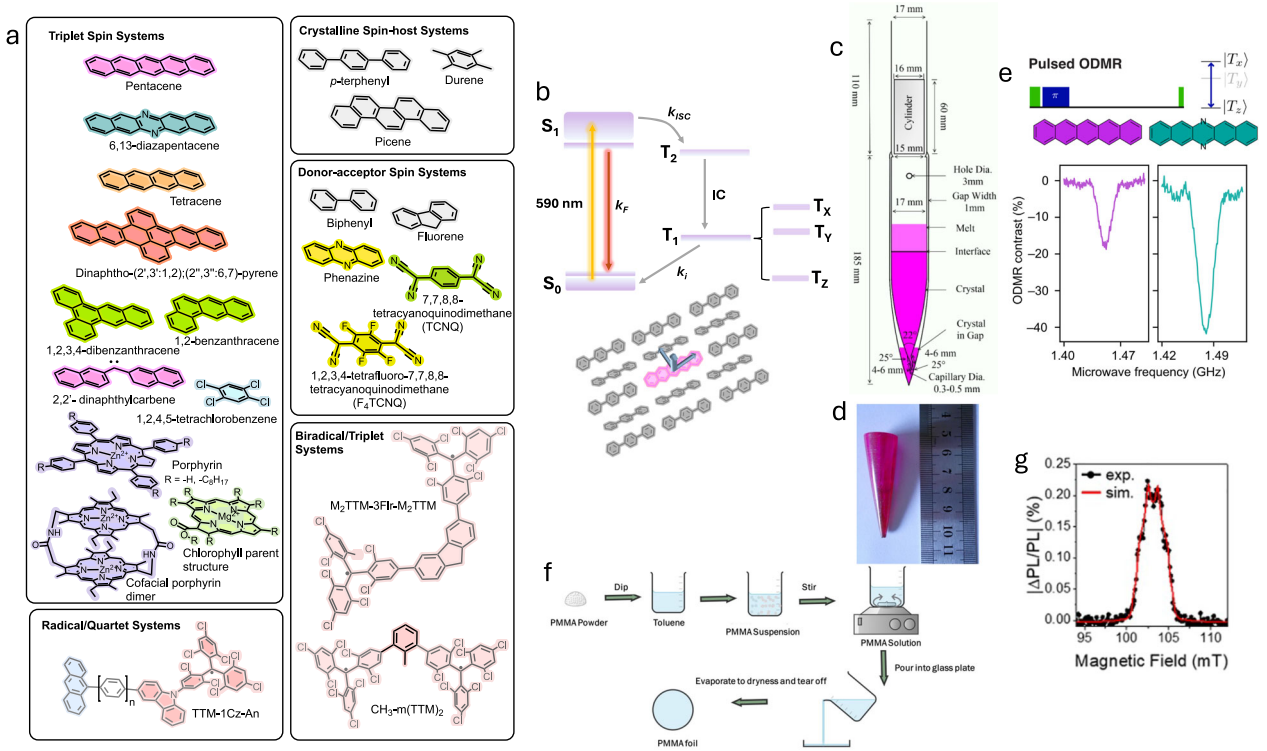


Fig. 7 | Fully optically addressable organic quantum materials. a Molecular structures of known organic FOAMs. **b** Jablonski diagram for ground-singlet state materials, like Pc:PTP, with an inset doped structure crystal of p-terphenyl. The materials are excited/initialised using light. The spin centres subsequently relax by fluorescence (k_F) or populating the triplet states through intersystem crossing (k_{ISC}). Repopulation of the singlet ground state occurs in a triplet sub-level dependent manner (k_i, where i is the corresponding triplet sub-level) and gives rise to high-contrast spin-optical signals. **c** Bridgmann growth set up to manufacture doped organic crystals. **d** An example of a Bridgmann-grown single crystal of Pc:PTP. **e** ODMR spectrum of Pc:PTP and DAP:PTP demonstrates enhanced pulsed optical contrast due to modified spin dynamics. **f** Synthesis methodology to generate optically clear films (aka "foils") of doped PMMA as an excellent amorphous host for radicals with spin-optical readout. **g** An example ODMR spectrum of CH_3-m(TMM)$_3$ in a PMMA host. Figure 1**c**–**g** were reproduced from refs. 126,136,141,210 with permission from MDPI and the American Chemical Society under the open access Creative Commons licence.

power, and whilst the origin of this behaviour is still largely unknown, defects in multilayer hBN which are more protected from the environment are less prone to blinking[104]. This suggests that atmospheric control may be a sensible approach to improve the reliability of spin-dependent luminescent readout.

Molecular FOAMs

p-block molecular spin centres. Molecular systems are becoming increasingly popular and offer an enticing opportunity to develop chemically tunable quantum materials catered to different applications[105–108]. Ground-up synthesis enables the incorporation of particular functionalities such as stable radicals[109,110], modulation of triplet/singlet yields, enrichment with low or zero nuclear magnetic moments such as deuterium, oxygen and sulphur, or the targeted inclusion of nuclear spin-active elements such as nitrogen, phosphorous, transition metals, and lanthanides (vide infra). A synthetic approach also enables changes to the host matrix[111], spin concentration, defect orientation, and material processing approaches, which are limited for defect-based systems.

The first examples of ODMR performed on molecular systems focused on small organic molecules[112,113] and biologically relevant porphyrin molecules such as those found in chlorophyll and bacterial reaction centres. These molecules use photoexcited triplet states as the magnetically-active spin centres that spin-selectively relax through phosphorescence, or relax to the fluorescent single states[114,115] (Fig. 7a, b). Porphyrins may be coordinated with Mg^{2+} or Zn^{2+} ions, which, though affecting the yield of the photo-excited spin state, do not themselves directly harbour it due to their filled s- or d-orbitals. Until recently, studies on p-block FOAMs were typically limited to cw measurements at cryogenic temperatures and aimed at investigating the interplay between ground and excited states, the influence of the stereochemistry of the porphyrin dimer molecules[116], and detecting triplet states in nanolayers[117]. A few groups did, however extend their work to pulsed measurements, including Breiland et al.[112], who measured the coherence properties of 1,2,4,5-tetrachlorobenzene in durene at 4 K, and found a T_2 of a few microseconds, which could be significantly extended to a millisecond or so using dynamic decoupling or spin-locking techniques.

Single-molecule ODMR spectroscopy of pentacene molecules in a para-terphenyl matrix (Pc:PTP) has already been demonstrated at cryogenic temperatures in a series of remarkable works by Wrachtrup and colleagues[118–120]. Only recently have pulsed experiments been performed to reveal contrast and spin coherence properties that are competitive with materials like NV − diamond at room temperature. The T_x-T_y spin transition of a 0.1% crystal of Pc:PTP, grown using the Bridgman technique (Fig. 7c, d), demonstrates $T_1 \approx 23$ µs, $T_2 \approx 2.7$ µs and $T_2^* \approx 500$ ns[121,122]. Investigations using the more strongly spin-polarised T_x-T_z transition in both crystals and 100 nm-thin films at 0.01% and 0.1%, respectively, reveal similar spin dynamics and also suggest an ability to modulate Pc:PTP's spin properties according to sample thickness and spin concentration[123]. These robust spin-optical properties can be maintained in Pc:PTP nanocrystals down to 200 nm with an optical contrast similar to equivalently sized NV-diamond nanoparticles[124]. When coated with a Pluronic F-127 polymer, these nanoparticles also display excellent biocompatibility with low toxicity over 72 hours according to in vitro explorations, paving the way for their use in cell assay techniques.

The potential of using synthetic chemistry to modulate the spin dynamics to improve spin-optical properties has also been explored (see Fig. 7b). Substituting two carbon atoms on pentacene for nitrogen atoms resulted in 6,13-diazapentacene, which could be doped into a para-terphenyl host (DAP:PTP) by crystal growth and vapour deposition

techniques[125,126]. While maintaining a relatively long T_2 of 1.46 μs and strong triplet spin polarisation, DAP:PTP exhibited an enhanced contrast of up to 40%, surpassing the state of the art in NV-diamond platforms[126] (Fig. 7e). This improvement was attributed to the introduction of new low-energy non-bonding states that enhance vibrationally-induced spin-orbit coupling between the ground-state singlet and the metastable T_x state. It was also shown that direct solvent techniques can be used to grow ODMR-active DAP:PTP nanoparticles, which could be compatible with in vitro sensing experiments.

Further organic systems have demonstrated potential as optically addressable materials, though, to our knowledge, pulsed optically detected experiments have yet to be performed. For example, the room temperature steady-state ODMR contrast of a 1% crystal of pentacene-doped picene has been measured at 15%, representing a potentially significant improvement over the PTP matrix[127]. Steady-state ODMR signals have also previously been reported at 2 K for (perdeutero)tetracene, 1,2-benzathracene, 1,2,3,4-dibenzanthracene[128] and dinaphtho-(2',3':1,2);(2",3":6,7)-pyrene[129]. Interestingly, work by Corvaja, Pasimeni and Giometti et al. has shown that even highly spin-dense charge-transfer (CT) co-crystals can exhibit bright room temperature ODMR signals. Co-crystals comprised of donors such as biphenyl, fluorene, phenazine and acceptors such as 7,7':8,8'-tetracyanoquinodimethane (TCNQ) and 1,2,3,4-tetrafluoro-TCNQ (F_4TCNQ) have been studied to elucidate their triplet state dynamics[130,131]. These materials exhibit narrow resonance lines due to intermolecular site hopping of triplet excitons. The resonances for each site can become resolved at low temperatures where hopping is not thermodynamically favoured[130]. Their high-spin densities (≈50%) are highly advantageous for quantum sensing, where the a.c. Sensitivity is proportional to the $\sqrt{n_{spin}}$, though this is often concurrent with less robust quantum spin properties compared with dilute materials such as Pc:PTP. Moreover, these materials are also promising hosts for the study of exotic spin behaviours like singlet fission and triplet-triplet annihilation[132]. For example, at room temperature, the triplet states of phenazine:TCNQ are predominantly formed by singlet fission and using transient nutation EPR spectroscopy, the authors estimate T_1 and T_2 times of ≈1 μs and 600 ns, respectively, even at room temperature[133].

Several ground-state radical and diradical materials with an optical readout capacity have also been demonstrated[134–136], as have materials with quintet states[137–139]. Diradical materials have the advantage of exhibiting a ground-state triplet, making their optical addressability protocol identical to NV-diamond. Optical readout is enabled by employing luminescent radical moieties based on tris(2,4,6-trichlorophenyl)methyl (TTM)[140], where the radical is sterically isolated on a carbon atom with only weak hyperfine coupling to neighbouring ^{13}C and hydrogen atoms. As a result, these materials can benefit from relatively narrow resonance linewidths, long T_1s, and can be embedded in frozen solutions or optically transparent PMMA foils through simple solvent-based methods[141] (Fig. 7f, g).

Additionally, ODMR has long been used to investigate genuine biomolecules such as nucleotides and proteins using phosphorescence of pyridine dinucleotides or certain amino acid residues such as tryptophan[114,142], albeit at cryogenic temperatures. The emission wavelength-dependence of tryptophan's ZFS parameters enabled investigators to distinguish between different proteins and even different tryptophan residues in the same protein molecule. The usefulness of these studies was restricted due to the perceived inability of these molecules to maintain long T_1s at room temperature, where dynamic effects occur. However, recently, fluorescent proteins have been demonstrated as a viable spin-qubit medium in vivo and in solution at room temperature. Feder et al. used ODMR spectroscopy to demonstrate that at 80 K the X-Z and Y-Z triplet transitions of enhanced yellow fluorescent protein demonstrated a 44% and 32% ODMR contrast, respectively[143]. This corresponds with a zero-applied field T_1 of 141 μs (estimated from spin polarisation decay) and T_2 of 1.5 μs. Using Carr-Purcell-Meiboom-Gill (CPMG) dynamical decoupling, the effective decoherence time (T_{DD}) reached 16 μs. The authors largely circumvent overhead limitations from long triplet lifetimes (ms) using an additional near-infrared pulse to induce T_1 to T_2 transitions to induce reverse ISC and delayed fluorescence from S_1. This interesting methodology could be suitable for other spin systems with quasi-resonant S_1 and T_2 electronic states, such as pentacene, to increase their sensitivity by increasing measurement repetition rates.

d-block molecular spin centres. Optically addressable d-block molecules have been investigated for several decades, though due to the weak oscillator strength of forbidden d-d transitions, the majority of ODMR studies focused on luminescence stemming from ligand-based triplet states generated following intramolecular ligand-to-ligand or metal-to-ligand charge transfer events[115,144]. These studies have generally focused on the use of diamagnetic heavy metal centres such as Pd^{2+}, Gd^{2+}, Rh^{2+}, Au^{+}[145] where the extent of the metal-ligand orbital mixing is reduced. However, for elements with partially filled d-orbitals, the strong SOC stemming from the heavy metal centres plays a significant role in determining the spin-polarisation, spin-relaxation, and ZFS parameters. Accordingly, cryogenic temperatures are required to maintain the detectable transitions due to the strong SOC effects of the metal centres. One of the first attempts to investigate the quantum spin properties of these materials focused on Rh^{3+} biphenyl-type chelating ligands, where T_m was measured at a few microseconds at 1.4 K[146,147]. Due to the deeply cryogenic conditions, T_1-type processes were assumed to be negligible.

In the early 2000s, further ODMR studies of transition metal complexes became far more scarce before lighter metal complexes regained attention in the 2010s. However, optically addressable materials with first row transition metal-spin centres were first reported using tris(aceylacetonato)Cr^{3+} (acac) supported in an $Al(acac)_3$ crystalline host matrix at 1.9 K. While the ODMR properties of the $S = 3/2$ ground state are not reported, on-resonance excitation to the lowest energy doublet state is sufficient to generate spin polarisation, with the ODMR signal detected through the vibronic side bands[148], making it a molecular analogue of earlier ruby ODMR experiments[149].

Optically addressable d-block molecules with a ground-state and zero-applied magnetic field spin manifold have only recently been demonstrated with Cr^{4+} (Fig. 8a). The Cr^{4+} spin-centre was realised with several tolyl-based ligand systems where modifications to the ligand structure and corresponding ligand-field strength can be used to control optical excitation frequency and the ZFS of the Cr^{4+} $S = 1$ ground state[150] (Fig. 8b, c). To reduce intermolecular dipole coupling, the spin-active moiety is diluted in a matrix with the $S = 0$ isostructural tin analogue in crystals grown from hexane solutions[151]. Optical spin polarisation is then achieved by exciting molecular spins from the $S = 1$ state to the $S = 0$ manifold, which fluorescently decays within a few microseconds to favourably populate the $T_{\pm}$ states. Initial pulsed-ODMR experiments were performed on Cr^{4+}(o-tolyl)$_4$ spins, which benefit from an $E = 0$ triplet and a relatively long T_1 of 0.22 ms and T_2 of 640 ns at 5 K. This permits several optical cycles to build spin polarisation and enhance the optical contrast up to 14%. The coherent properties can be significantly improved using a non-isostructural Sn(4-fluoro-2-methylphenyl)$_4$ host matrix[152]. Here, the ZFS is significantly increased, giving rise to clock transitions similar to those realised by the so-called "zero first-order Zeeman" (ZEFOZ) method, initially pioneered for lanthanide spin systems (see below). As a result, T_1 and T_2 are increased to ≈1.21 ± 0.02 ms and ≈10.6 ± 0.2 μs at 5 K, respectively, while the pulsed contrast can be improved up to 65%.

Work continues to explore alternative d-block elements where strong ligand-field interactions can enable optical excitation between spin manifolds and spin-dependent fluorescence[105,108]. Candidates include Ni^{2+}[153,154], Mo^{4+}[155], V^{3+}[155,156]. Current challenges involve tuning the energy of the intermediate (e.g., singlet) state to provide the right conditions for spin polarisation, and identifying the appropriate ligand design to optimise photoluminescence.

f-block molecular spin centres. Lastly, there has been significant interest in f-block molecular systems. Here, we make a distinction between molecular systems where the ion is doped into a molecular

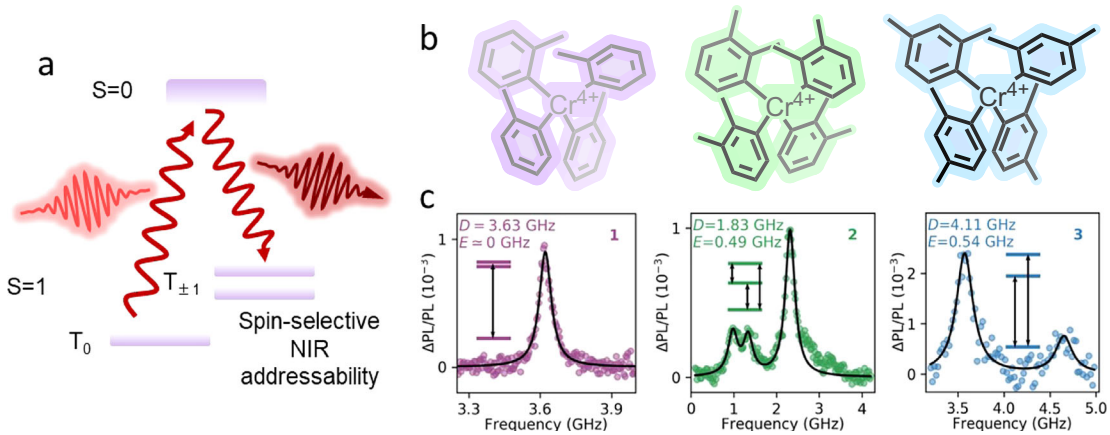


Fig. 8 | Optically addressable Cr^{4+} molecular colour centres. a Energy level illustration of spin initialisation and readout using resonant NIR-photoinduced ISC from the ground state triplet to an excited singlet state, followed by spin-selective fluorescence to $T_{\pm}$ spin sublevels. **b** Molecular structures of three Cr^{4+} tolyl-type complexes, and **c** their corresponding cw-ODMR signals. **a**, **c** were adapted from ref. 151.

lattice, and trapped ion systems where a single ion is levitated using electrostatic interactions to give rise to extremely long coherence times, but are not subject to qubit-quality improvements through molecular engineering[157–159].

Lanthanide spin centres benefit from highly shielded f-orbital electrons compared to d-orbital systems, leading to relatively long coherence times at low temperatures[160]. The core-like nature of f-orbitals also means, compared to d-orbital systems, that the ligand-field environment has a much weaker influence on state energies (a few THz), compared to electron-electron interactions (≈800–1600 nm) and spin-orbit coupling (≈10s THz)[161,162] (see Fig. 9a). Lanthanide electron spins can also exhibit strong hyperfine coupling (tens of MHz) with $I = 5/2$ (Eu, Pr, ^{173}Yb), $I = 1/2$ (^{171}Yb), $I = 7/2$ (^{149}Sm, ^{167}Er) nuclei, leading to a diverse spin-optical addressability schemes that can be further enhanced using applied magnetic fields. Moreover, strong spin-orbit coupling can lead to high magnetic anisotropy that can protect spin states from small magnetic fluctuations[163,164]. Examples of optically active materials benefit from narrow and stable spin-dependent emission profiles at near-infrared frequencies, making them potentially compatible with conventional telecom fibre optics. Colour centres for which optical addressability has been established include Ce^{3+}[165], Eu^{3+}-[166], Pr^{3+}-[167], Er^{3+}-[3], Yb^{3+}-[168], and Sm^{3+}:Y_2SiO_5[169] (Fig. 9c).

In the solid-state, Y_2SiO_5 has been favoured as host matrix due to the ability to grow large crystals with excellent optical properties using the Czochralski method[170] (Fig. 9b). However, as the only naturally occurring isotope, ^{89}Y harbours an $I = 1/2$ nuclear spin that ultimately limits decoherence times. To reduce the impact of the spin bath, various decoupling techniques have emerged[171–173]. Perhaps the most successful is the so-called "ZEFOZ" technique, whereby a magnetic field is applied such that the magnetic field dependence of the spin-transition frequency is very close to zero[174] (Fig. 9d). In this "clock transition" regime, spins are first-order insensitive to small fluctuations in local magnetic fields. Using this technique with Eu^{3+}:Y_2SiO_5, Zhong et al. demonstrated that it is possible to acquire $T_2 \gg 100$ ms at 2 K, where spin-phonon coupling is negligible. Remarkably, combined with dynamic decoupling methods, T_{DD} was measured to be 370 ± 60 mins, reaching a critical milestone whereby the distance-dependent decoherence becomes less for spin-transport than it is during light-transport of quantum states[175].

Interestingly, the larger magnetic moment of Pr^{3+} can give rise to "frozen core"-type behaviour, whereby local Y-spins become dephased from the bulk crystal and hence exhibit reduced dephasing influence on the Pr^{3+} spins[171]. Equall et al. measured homogenous field-dependent and crystal structure site-dependent linewidths between 2.5 and 0.85 kHz, and a corresponding T_2 as high as 377 µs at 1.4 K[167]. Combined with the ZEFOZ method, the T_2 can reach 82 ms at 1.5 K[171] (see example Fig. 9e), and with further dynamical decoupling T_{DD} up to 1 min can be achieved, approaching the population lifetime limit[176]. Coherence times can also be enhanced using a host matrix whereby the principal host ion (e.g., Y) has a more closely matched ionic radius to the dopant, leading to reduced crystallographic distortions. For example, in a Pr^{3+}:$La_2(WO_4)_3$ system, a T_2 of 158 ± 7 ms has been measured at ≈ 4 K[177].

Spin coherence times of Er^{3+}:Y_2SiO_5 have so far been shorter than the best-performing Eu^{3+} materials, with T_2 measured at 1.3 ± 0.01 seconds at 1.4 K, despite exhibiting the frozen core effect[3]. However, this was achieved without using the ZEFOZ method, and therefore, these times can likely be significantly extended. Er^{3+} has also been studied in a Y_2O_3 host with T_2 reaching ≈140 µs at 1.8 K and with an applied field of 4 T[178]. Decoherence was dominated by phonon-driven dipole-dipole interactions and the nuclear spin bath at high fields, similar to Er^{3+}:$KTiOPO_4$ where T_2 was measured at ≈ 200 µs under similar conditions[179].

$^{171}Yb^{3+}$ holds a unique position amongst the lanthanide ions discussed so far due to its $S = 1/2$ and $I = 1/2$ electron spin and hyperfine structure, resulting in a simple 4-level system. Of the $^{171}Yb^{3+}$-doped materials[180], $^{171}Yb^{3+}$:Y_2SiO_5 appears to exhibit the longest spin coherence times. This material was initially studied by X-band EPR spectroscopy and presented with an electron T_1 of ≈5 seconds at 2.5 K with an applied field of ≈90 mT. T_1 quickly increases above ≈4 K due to Raman relaxation, where T_2 becomes ultimately limited by T_1[181]. At 2.5 K, T_2 was optimised at ≈ 1 T to 73 µs and improved further by dynamical decoupling, reaching 550 µs. In the same experiments, the authors record nuclear T_1 and T_2 at 4.5 K of 4 and 0.35 ms, respectively. Using an optical approach, Ortu et al. improved the coherent properties of $^{171}Yb^{3+}$:Y_2SiO_5 by employing the ZEFOZ method such that the electron T_2 remains above 100 µs at 5.6 K, and the nuclear T_2 extends to 1 ms[168]. Using a different approach, Welinski et al. demonstrated that coherence can also be extended by first polarising host nuclear spins through spin diffusion. At 2 K, the authors first excite ^{171}Yb spins before allowing them to equilibrate over a few seconds through spectral diffusion over the inhomogeneous linewidth. The result is an effective "hole burning" in the absorption spectrum of $^{171}Yb^{3+}$:Y_2SiO_5 and up to 90% nuclear spin polarisation, thereby effectively generating mK spin temperatures and improving the optical T_2 from 0.3 to 0.8 ms[182].

To our knowledge, pulsed optical decoherence studies have not been performed on Sm^{3+}:Y_2SiO_5, however, its $I = 7/2$ nucleus and strong hyperfine coupling may be useful for qudit systems, and it is also predicted to be less sensitive to magnetic field fluctuations than Er^{3+}[169,183].

Finally, in recent years, Ce^{3+}:YAG has become a well-studied example of a potential lanthanide spin material that is readily available. As with the previous V^{4+} and Mo^{2+} spin centres found in SiC, Ce^{3+} exhibits a $S = 1/2$ ground state and is not initialised through ISC, but rather uniquely uses left-

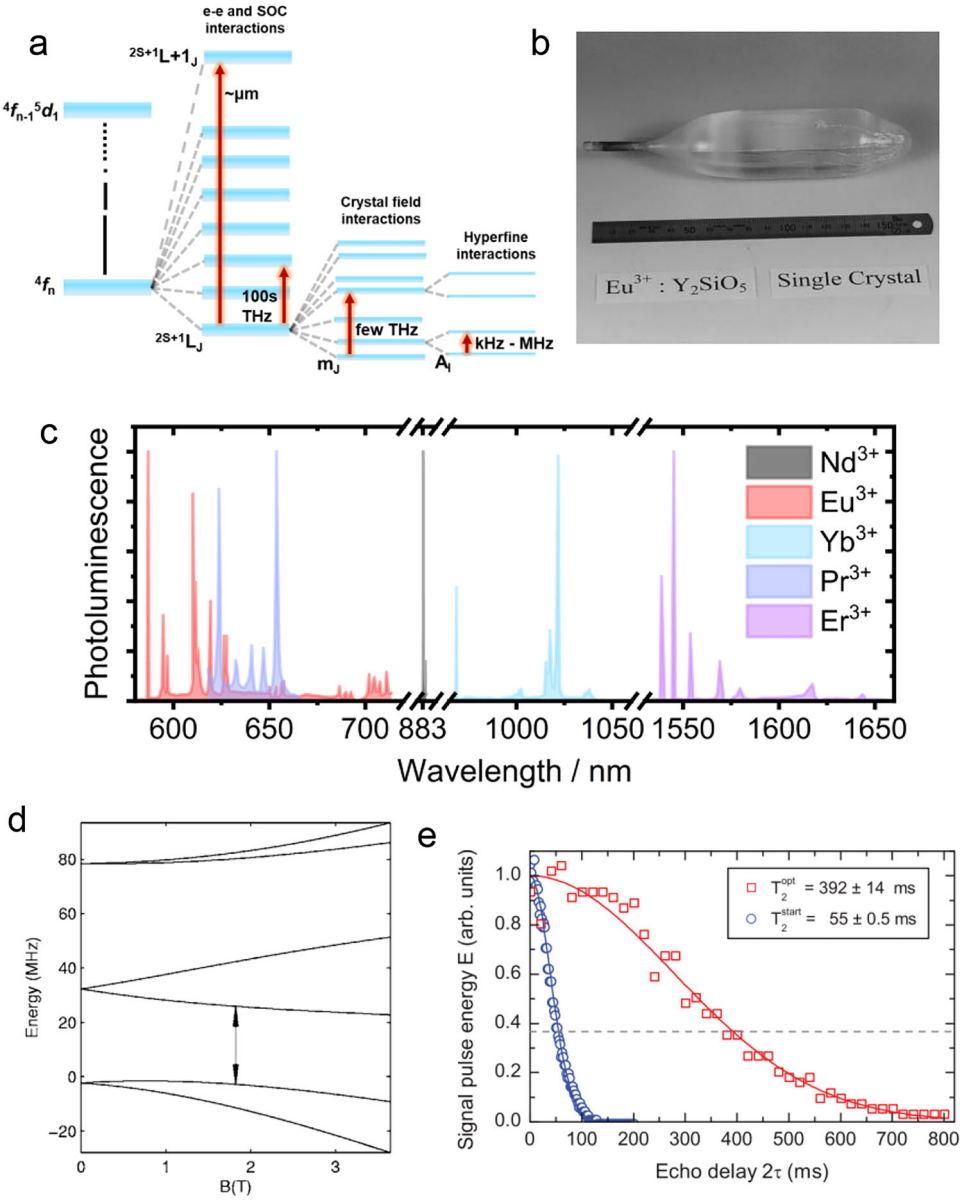


Fig. 9 | Optically addressable lanthanide spin qubits. a Generic energy level diagram showing energy level splitting due to electron-electron interactions (e-e, leading to $^{2S+1}$L states), spin-orbit coupling (SOC, *J*), crystal field (m_J) and hyperfine interactions (A_I). **b** Example single crystal of Eu^{3+}:Y_2SiO_4 grown by the Czochralski method. **c** Collated example photoluminescence spectra from purely inorganic lanthanide-doped crystal host systems demonstrating coverage of the visible and near-infrared spectrum. **d** Examples of a zero first-order Zeeman (ZEFOZ) transition for Eu^{3+}:Y_2SiO_5 spin system with the transition region indicated, demonstrating equal energy-field gradients, resulting in magnetic field insensitivity, and **e** impact of the ZEFOZ method on spin decoherence time for Pr^{3+}:Y_2SiO_5 showing T_2^{start} without ZEFOZ and T_2^{opt} with ZEFOZ. **b**, **d**, **e** were reproduced from refs. 170,176,211, respectively, with permission from the American Physical Society and Elsevier. Data points for (**c**) were extracted from refs. 166,167,175,180,212.

or right-handed circularly polarised light to selectively depopulate a spin-dependent ZPL[184]. Moreover, unlike many lanthanide defects, this 4f- to 5d-orbital transition exhibits a high oscillator strength and can be excited using green light with yellow emission, generating a theoretical maximum of 99.7% spin polarisation in its excited state. This state only lasts ≈63 ns or so before relaxing back to the ground state with a reported ODMR contrast of 98%[185]. Whilst maintenance of robust spin properties still requires low temperatures, in part due to the abundance of ^{27}Al ($I = 5/2$) in the YAG[186,187], detectable spin coherence is maintained up to 20 K–significantly higher than other lanthanides, and T_1 can even be measured at room temperature[184]. Cross relaxation of commonly found co-impurities has been used to optically read out the spin-state of species like Tb^{3+} and Gb^{3+}[188,189], demonstrating the capacity of Ce^{3+} to act as a spin readout relay for otherwise dark spins - an essential property for nanoscale sensing. Moreover, Ce^{3+}:YAG may even demonstrate improved ODMR spin properties when manufactured into thin films, making it a promising platform for incorporation into devices[190].

Optimising performance of spin-qubit materials

From our review, it is clear that spin-based qubit candidates demonstrate potential in several fields of quantum technology. However, unsurprisingly, their spin coherence lifetimes are limited by temperature and the spin-bath dependence of the spin properties and optical contrast between different spin states. Across all material platforms, there is significant magnetic inhomogeneity that emerges from random local spin environments. To understand the extent to which inhomogeneity infects different materials, it could be instructive to consider the ratio of T_2^*/T_2 (Fig. 10, the so-called "inhomogeneity parameter"). Hence, a low ratio indicates that T_2 is close to T_2^* and the materials are limited by dynamic, not static, sources of decoherence. Using the available data where T_2^* and T_2 were measured under similar conditions, there appears to emerge a distinct advantage for molecules and van der Waals materials at higher temperatures despite their lack of isotopic enrichment. This likely stems from the use of molecular crystals and the inherent 2D-order associated with materials such as hBN, which helps to ensure that all molecules "feel" the same magnetic environment. Interestingly, despite the significant difficulties associated with synthesising aligned 3D spin defects in diamond, SnV^-diamond (measured as single spins) exhibits the lowest ratio at low temperatures. Considering its robust quantum spin parameters, SnV^-diamond could be a leading candidate for low-temperature applications.

Spin parameters can be improved by positional engineering of defect centres. Clustering (or the straggling) of spin-active dopants in a substrate

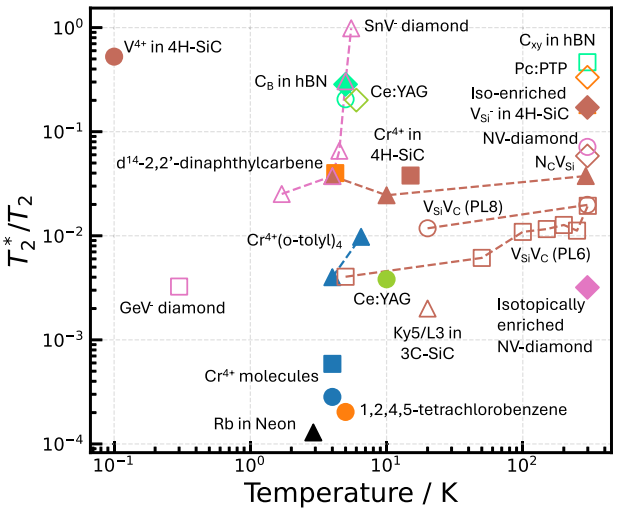


Fig. 10 | Comparison of T_2 and T_2^* for different spin systems as a measure of inhomogeneity. This ratio generally grows with temperature due to an increasing prevalence of dynamic decoherence including phonons and Johnson-Nyquist noise.

poses spin-spin coupling from the environment (nuclear spins), which decreases T_2. Controlled doping becomes crucial in decreasing spin density around spin-active defect centres. Eliminating unwanted spins like nuclear spins requires isotopic purity of substrate material or the careful doping of spin-active centres or defects within the host matrix. More recently, Plasma-Enhanced CVD methods have been used to achieve higher deposition rates while minimising the impact of energetic ions or electrons affecting the colour centres in NV and SnV diamonds[191]. Another novel method to precisely control the position of each defect is laser writing. Aberration-corrected optics allow for the precise positioning of vacancies in diamond systems, with a 45% success probability of a vacancy being located within 200 nm of a desired position[192].

Due to their ability to effectively engineer the placement of molecules in 3D chemical systems, materials with charge transfer or hydrogen bonding motifs may yet demonstrate advantages. Moreover, as seen with Pc:PTP, and Pr^{3+}:Y_2SiO_5 vs. the $La_2(WO_5)_3$ host, material engineers should avoid defect-site strain by selecting hosts with closely matched physical parameters to the defect. Finally, further improvements can be realised through dynamical decoupling methods that are tailored for each application. For example, while engineering clock transitions using magnetic fields or ZFS is appealing for quantum optics where spectral stability is prised, it is not necessarily useful for sensing or information processing. This is because the associated reduced magnetic field sensitivity would reduce the quantum operation fidelity. On the other hand, focused electromagnetic driving of parasitic impurities, such as N-centres in diamond, has yet to be significantly explored in molecular systems. Significant improvements in T_2 and T_2^* would likely emerge from a combination of field-driving and pulsed refocusing methods such as CPMG.

Conclusion and outlook

Optically addressable spin systems show great potential as a diverse form of qubit media for quantum sensing, communications, and information processing applications. From this review, we have attempted to benchmark the different families of materials and identify useful investigative and experimental approaches that can be translated across the field. The most significant hurdles faced by chemists and materials engineers remain the strong temperature dependence of the spin-lattice relaxation and thermal polarisation of the spin bath, which renders most heavy atom-containing systems impractical above a few kelvin, but below which these materials demonstrate the longest coherence times by a significant margin. However, above liquid helium temperatures, it is clear that light-element materials such as colour centres in diamond, SiC and most recently, molecular systems demonstrate more robust quantum spin parameters. Nevertheless, significant advancements in dynamic decoupling techniques within the last 20 years and isotope engineering have enabled the realisation of remarkably competitive quantum spin properties. Within the next decade, it is expected that further advances and knowledge transfer between investigators of different material platforms will lead to devices capable of significantly impacting society, especially in the field of magnetic field sensors and coherent quantum optics. In particular, materials that are currently prised for their spectral stability and employed mainly for applications in quantum optics and communication or networking (e.g., f-block, heavy atom vacancy centres) will benefit from incorporating the relatively weak phononic sensitivity and high brightness found in materials primarily used for quantum sensing and information processing (e.g., defects in diamond, SiC, hBN and molecules), and vice versa. We also hope that by collating (meta)data on the available spin-qubit candidates, the field will eventually benefit from the processing and predictive power of machine learning and artificial intelligence approaches to materials discovery.

Data Availability

All data used in this review is available in the supplementary data in .xlsx format.

Received: 1 July 2025; Accepted: 22 March 2026;
Published online: 05 April 2026

References

1. Castelvecchi, D. IBM releases first-ever 1,000-qubit quantum chip. *Nature* https://www.nature.com/articles/d41586-023-03854-1 (2023).
2. Pino, J. M. et al. Demonstration of the trapped-ion quantum CCD computer architecture. *Nature* **592**, 209–213 (2021).
3. Rančić, M., Hedges, M. P., Ahlefeldt, R. L. & Sellars, M. J. Coherence time of over a second in a telecom-compatible quantum memory storage material. *Nat. Phys.* **14**, 50–54 (2018).
4. Brilliance, Q. This german startup wants to build portable quantum computers using diamonds - and says its qpu will sit next to a gpu or a cpu one day. *TechRadar* https://quantumbrilliance.com/news-media (2025).
5. Barry, J. F. et al. Sensitivity optimization for NV-diamond magnetometry. *Rev. Mod. Phys.* **92**, 015004 (2020).
6. Chizzini, M. et al. Quantum error correction with molecular spin qudits. *Phys. Chem. Chem. Phys.* **24**, 20030–20039 (2022).
7. Arecchi, F. T., Courtens, E., Gilmore, R. & Thomas, H. Atomic coherent states in quantum optics. *Phys. Rev. A* **6**, 2211–2237 (1972).
8. DiVincenzo, D. P. & Loss, D. Quantum computers and quantum coherence. *J. Magn. Magn. Mater.* **200**, 202–218 (1999).
9. DiVincenzo, D. P. The physical implementation of quantum computation. *Fortschr. Phys.* **48**, 771–783 (2000).
10. Bergli, J., Galperin, Y. M. & Altshuler, B. L. Decoherence in qubits due to low-frequency noise. *N. J. Phys.* **11**, 025002 (2009).
11. Traficante, D. D. Relaxation: Can T_2 be longer than T_1? *Concepts Magn. Reson.* **3**, 171–177 (1991).
12. Chavhan, G. B., Babyn, P. S., Thomas, B., Shroff, M. M. & Haacke, E. M. Principles, techniques, and applications of T_2^*-based MR imaging and its special applications. *RadioGraphics* **29**, 1433–1449 (2009).
13. Chirolli, L. & Burkard, G. Decoherence in solid-state qubits. *Adv. Phys.* **57**, 225–285 (2008).
14. Roberts, H., Abudayyeh, H., Li, X. & Li, X. Quantum sensing with spin defects beyond diamond. *ACS Nano* https://pubs.acs.org/doi/10.1021/acsnano.5c00802 (2025).
15. Weber, J. R. et al. Quantum computing with defects. *Proc. Natl. Acad. Sci.* **107**, 8513–8518 (2010).
16. Mrózek, M. et al. Longitudinal spin relaxation in nitrogen-vacancy ensembles in diamond. *EPJ Quantum Technol.* **2**, 22 (2015).

17. Cambria, M. C. et al. Temperature-dependent spin-lattice relaxation of the nitrogen-vacancy spin triplet in diamond. *Phys. Rev. Lett.* **130**, 256903 (2023).
18. Norambuena, A. et al. Spin-lattice relaxation of individual solid-state spins. *Phys. Rev. B* **97**, 094304 (2018).
19. Zhang, W. et al. Depth-dependent decoherence caused by surface and external spins for NV centers in diamond. *Phys. Rev. B* **96**, 235443 (2017).
20. Stanwix, P. L. et al. Coherence of nitrogen-vacancy electronic spin ensembles in diamond. *Phys. Rev. B* **82**, 201201 (2010).
21. Tsuji, T., Sekiguchi, T., Iwasaki, T. & Hatano, M. Extending spin dephasing time of perfectly aligned nitrogen vacancy centers by mitigating stress distribution on highly misoriented chemical vapor deposition diamond. *Adv. Quantum Technol.* **7**, 1–8 (2024).
22. Luo, T. et al. Creation of nitrogen-vacancy centers in chemical vapor deposition diamond for sensing applications. *N. J. Phys.* **24**, 033030 (2022).
23. Zhang, X. et al. Highly coherent nitrogen vacancy centers in diamond via rational high pressure and high temperature synthesis and treatment. *Adv. Funct. Mater.* **33**, 1–9 (2023).
24. Takahashi, S., Hanson, R., van Tol, J., Sherwin, M. S. & Awschalom, D. D. Quenching spin decoherence in diamond through spin bath polarization. *Phys. Rev. Lett.* **101**, 047601 (2008).
25. Balasubramanian, G. et al. Ultralong spin coherence time in isotopically engineered diamond. *Nat. Mater.* **8**, 383–387 (2009).
26. Chen, X.-D. et al. Spin depolarization effect induced by charge state conversion of nitrogen vacancy center in diamond. *Phys. Rev. B* **92**, 104301 (2015).
27. Cardoso Barbosa, I. Impact of charge conversion on NV-center relaxometry. *Phys. Rev. B* **108**, 184102 (2023).
28. Thiering, G. & Gali, A. Color centers in diamond for quantum applications. *Semicond. Semimetals* **103**, 1–36 (Elsevier, 2020).
29. Komarovskikh, A., Nadolinny, V., Palyanov, Y., Kupriyanov, I. & Sokol, A. EPR study of the hydrogen center in HPHT diamonds grown in carbonate medium. *Phys. Status Solidi* **211**, 2274–2278 (2014).
30. Umeda, T. et al. Negatively charged boron vacancy center in diamond. *Phys. Rev. B* **105**, 165201 (2022).
31. Hartland, C. B. *A Study of Point Defects in CVD Diamond Using Electron Paramagnetic Resonance and Optical Spectroscopy*. PhD thesis, Univ. Warwick (2014).
32. Bradac, C., Gao, W., Forneris, J., Trusheim, M. E. & Aharonovich, I. Quantum nanophotonics with group IV defects in diamond. *Nat. Commun.* **10**, 5625 (2019).
33. Pingault, B. et al. Coherent control of the silicon-vacancy spin in diamond. *Nat. Commun.* **8**, 15579 (2017).
34. Chen, C., Jiang, B. & Hu, X. Research progress on silicon vacancy color centers in diamond. *Funct. Diam.* **4**, 2332346 (2024).
35. Görlitz, J. et al. Coherence of a charge stabilised tin-vacancy spin in diamond. *npj Quantum Inf.* **8**, 45 (2022).
36. Karapatzakis, I. et al. Microwave control of the tin-vacancy spin qubit in diamond with a superconducting waveguide. *Phys. Rev. X* **14**, 31036 (2024).
37. Iwasaki, T. et al. Germanium-vacancy single color centers in diamond. *Sci. Rep.* **5**, 12882 (2015).
38. Trusheim, M. E. et al. Lead-related quantum emitters in diamond. *Phys. Rev. B* **99**, 075430 (2019).
39. Wang, P. et al. Transform-limited photon emission from a lead-vacancy center in diamond above 10 K. *Phys. Rev. Lett.* **132**, 073601 (2024).
40. Morris, I. et al. Lifetime-limited and tunable emission from single charge-stabilized nickel vacancy centers in diamond. *Phys. Rev. Lett.* **135**, 043602 (2025).
41. Mohseni, M., Razinkovas, L., Žalandauskas, V., Thiering, G. & Gali, A. Magneto-optical properties of group-iv vacancy centers in diamond upon hydrostatic pressure. *Phys. Rev. B* **112**, 155201 (2025).
42. Meesala, S. et al. Strain engineering of the silicon-vacancy center in diamond. *Phys. Rev. B* **97**, 205444 (2018).
43. Waltrich, R., Klotz, M., Agafonov, V. N. & Kubanek, A. Two-photon interference from silicon-vacancy centers in remote nanodiamonds. *Nanophotonics* **12**, 3663–3669 (2023).
44. Sohn, Y.-I. et al. Controlling the coherence of a diamond spin qubit through its strain environment. *Nat. Commun.* **9**, 2012 (2018).
45. Green, B. L. et al. Neutral silicon-vacancy center in diamond: spin polarization and lifetimes. *Phys. Rev. Lett.* **119**, 096402 (2017).
46. Senkalla, K., Genov, G., Metsch, M. H., Siyushev, P. & Jelezko, F. Germanium vacancy in diamond quantum memory exceeding 20 ms. *Phys. Rev. Lett.* **132**, 026901 (2024).
47. Rosenthal, E. I. et al. Microwave spin control of a tin-vacancy qubit in diamond. *Phys. Rev. X* **13**, 031022 (2023).
48. Trusheim, M. E. et al. Transform-limited photons from a coherent tin-vacancy spin in diamond. *Phys. Rev. Lett.* **124**, 023602 (2020).
49. Thiering, G. & Gali, A. Magneto-optical spectra of the split nickel-vacancy defect in diamond. *Phys. Rev. Res.* **3**, 043052 (2021).
50. Fischer, M. et al. Highly efficient optical pumping of spin defects in silicon carbide for stimulated microwave emission. *Phys. Rev. Appl.* **9**, 054006 (2018).
51. Castelletto, S. et al. Silicon carbide photonics bridging quantum technology. *ACS Photonics* **9**, 1434–1457 (2022).
52. Harmon, K. J. et al. Designing silicon carbide heterostructures for quantum information science: challenges and opportunities. *Mater. Quantum Technol.* **2**, 023001 (2022).
53. Gottscholl, A. et al. Superradiance of spin defects in silicon carbide for maser applications. *Front. Photonics* **3**, 1–9 (2022).
54. Ou, H. Silicon carbide, the next-generation integrated platform for quantum technology. *Light Sci. Appl.* **13**, 219 (2024).
55. Castelletto, S., Lew, C. T., Lin, W.-X. & Xu, J.-S. Quantum systems in silicon carbide for sensing applications. *Rep. Prog. Phys.* **87**, 014501 (2024).
56. Castelletto, S. & Boretti, A. Silicon carbide color centers for quantum applications. *J. Phys.: Photonics* **2**, 022001 (2020).
57. Nagy, R. et al. High-fidelity spin and optical control of single silicon-vacancy centres in silicon carbide. *Nat. Commun.* **10**, 1954 (2019).
58. Wang, J.-F. et al. Coherent control of nitrogen-vacancy center spins in silicon carbide at room temperature. *Phys. Rev. Lett.* **124**, 223601 (2020).
59. Jiang, Z., Cai, H., Cernansky, R., Liu, X. & Gao, W. Quantum sensing of radio-frequency signal with NV centres in sic. *Sci. Adv.* **9**, eadg2080 (2023).
60. Koehl, W. F. et al. Resonant optical spectroscopy and coherent control of Cr^{4+} spin ensembles in SiC and GaN. *Phys. Rev. B* **95**, 035207 (2017).
61. Diler, B. et al. Coherent control and high-fidelity readout of chromium ions in commercial silicon carbide. *npj Quantum Inf.* **6**, 11 (2020).
62. Wolfowicz, G. et al. Vanadium spin qubits as telecom quantum emitters in silicon carbide. *Sci. Adv.* **6**, eaaz1192 (2020).
63. Ahn, J. et al. Extended spin relaxation times of optically addressed vanadium defects in silicon carbide at telecommunication frequencies. *Phys. Rev. Appl.* **22**, 044078 (2024).
64. Gilardoni, C. M. et al. Spin-relaxation times exceeding seconds for color centers with strong spin-orbit coupling in SiC. *N. J. Phys.* **22**, 103051 (2020).
65. Baur, J., Kunzer, M. & Schneider, J. Transition metals in SiC polytypes, as studied by magnetic resonance techniques. *Phys. Status Solidi* **162**, 153–172 (1997).
66. Simin, D. et al. Locking of electron spin coherence above 20 ms in natural silicon carbide. *Phys. Rev. B* **95**, 161201 (2017).
67. Babin, C. et al. Fabrication and nanophotonic waveguide integration of silicon carbide colour centres with preserved spin-optical coherence. *Nat. Mater.* **21**, 67–73 (2022).

68. Lekavicius, I. et al. Orders of magnitude improvement in coherence of silicon-vacancy ensembles in isotopically purified 4H-SiC. *PRX Quantum* **3**, 010343 (2022).
69. Christle, D. J. et al. Isolated electron spins in silicon carbide with millisecond coherence times. *Nat. Mater.* **14**, 160–163 (2015).
70. Falk, A. L. et al. Polytype control of spin qubits in silicon carbide. *Nat. Commun.* **4**, 1819 (2013).
71. Sun, T. et al. Divacancy and silicon vacancy color centers in 4H-SiC fabricated by hydrogen and dual ions implantation and annealing. *Ceram. Int.* **49**, 7452–7465 (2023).
72. Lee, E. M. Y., Yu, A., de Pablo, J. J. & Galli, G. Stability and molecular pathways to the formation of spin defects in silicon carbide. *Nat. Commun.* **12**, 6325 (2021).
73. Seo, H. et al. Quantum decoherence dynamics of divacancy spins in silicon carbide. *Nat. Commun.* **7**, 12935 (2016).
74. Yan, F.-F. et al. Room-temperature coherent control of implanted defect spins in silicon carbide. *npj Quantum Inf.* **6**, 38 (2020).
75. Klimov, P. V., Falk, A. L., Buckley, B. B. & Awschalom, D. D. Electrically driven spin resonance in silicon carbide color centers. *Phys. Rev. Lett.* **112**, 087601 (2014).
76. Lew, C. T.-K. et al. All-electrical readout of coherently controlled spins in silicon carbide. *Phys. Rev. Lett.* **132**, 146902 (2024).
77. Niethammer, M. et al. Coherent electrical readout of defect spins in silicon carbide by photo-ionization at ambient conditions. *Nat. Commun.* **10**, 5569 (2019).
78. Koller, P., Astner, T., Tissot, B., Burkard, G. & Trupke, M. Strain-enabled control of the vanadium qudit in silicon carbide. *Phys. Rev. Mater.* **9**, L043201 (2025).
79. Wolfowicz, G. et al. Vanadium spin qubits as telecom quantum emitters in silicon carbide. *Sci. Adv.* **6**, 2–9 (2020).
80. Cilibrizzi, P. et al. Ultra-narrow inhomogeneous spectral distribution of telecom-wavelength vanadium centres in isotopically-enriched silicon carbide. *Nat. Commun.* **14**, 8448 (2023).
81. Tissot, B., Trupke, M., Koller, P., Astner, T. & Burkard, G. Nuclear spin quantum memory in silicon carbide. *Phys. Rev. Res.* **4**, 033107 (2022).
82. Astner, T. et al. Vanadium in silicon carbide: telecom-ready spin centres with long relaxation lifetimes and hyperfine-resolved optical transitions. *Quantum Sci. Technol.* **9**, 035038 (2024).
83. Bosma, T. et al. Identification and tunable optical coherent control of transition-metal spins in silicon carbide. *npj Quantum Inf.* **4**, 48 (2018).
84. Shaik, A. B. D. -a-j-w-i & Palla, P. Optical quantum technologies with hexagonal boron nitride single photon sources. *Sci. Rep.* **11**, 12285 (2021).
85. Giest, D. & Romelt, G. Paramagnetische elektronenresonanz in bornitrid. *Solid State Commun.* **2**, 149 (1964).
86. Moore, A. & Singer, L. Electron spin resonance in carbon-doped boron nitride. *J. Phys. Chem. Solids* **33**, 343–356 (1972).
87. Katzir, A., Suss, J. T., Zunger, A. & Halperin, A. Point defects in hexagonal boron nitride. I. EPR, thermoluminescence, and thermally-stimulated-current measurements. *Phys. Rev. B* **11**, 2370–2377 (1975).
88. Exarhos, A. L., Hopper, D. A., Patel, R. N., Doherty, M. W. & Bassett, L. C. Magnetic-field-dependent quantum emission in hexagonal boron nitride at room temperature. *Nat. Commun.* **10**, 222 (2019).
89. Gottscholl, A. et al. Initialization and read-out of intrinsic spin defects in a van der Waals crystal at room temperature. *Nat. Mater.* **19**, 540–545 (2020).
90. Mathur, N. et al. Excited-state spin-resonance spectroscopy of V_B^- defect centers in hexagonal boron nitride. *Nat. Commun.* **13**, 1–7 (2022).
91. Gong, R. et al. Coherent dynamics of strongly interacting electronic spin defects in hexagonal boron nitride. *Nat. Commun.* **14**, 3299 (2023).
92. Gottscholl, A. et al. Room temperature coherent control of spin defects in hexagonal boron nitride. *Sci. Adv.* **7**, eabf3630 (2021).
93. Healey, A. J. et al. Optimisation of electron irradiation for creating spin ensembles in hexagonal boron nitride. *Mater. Quantum Technol.* **4**, 035701 (2024).
94. Hayee, F. et al. Revealing multiple classes of stable quantum emitters in hexagonal boron nitride with correlated optical and electron microscopy. *Nat. Mater.* **19**, 534–539 (2020).
95. Krečmarová, M. et al. Extrinsic effects on the optical properties of surface color defects generated in hexagonal boron nitride nanosheets. *ACS Appl. Mater. Interfaces* **13**, 46105–46116 (2021).
96. Chejanovsky, N. et al. Single-spin resonance in a van der Waals embedded paramagnetic defect. *Nat. Mater.* **20**, 1079–1084 (2021).
97. Stern, H. L. et al. Room-temperature optically detected magnetic resonance of single defects in hexagonal boron nitride. *Nat. Commun.* **13**, 1–9 (2022).
98. Stern, H. L. et al. A quantum coherent spin in hexagonal boron nitride at ambient conditions. *Nat. Mater.* **23**, 1379–1385 (2024).
99. M. Gilardoni, C. et al. A single spin in hexagonal boron nitride for vectorial quantum magnetometry. *Nat. Commun.* **16**, 4947 (2025).
100. Guo, N.-J. et al. Coherent control of an ultrabright single spin in hexagonal boron nitride at room temperature. *Nat. Commun.* **14**, 2893 (2023).
101. Scholten, S. C. et al. Multi-species optically addressable spin defects in a van der Waals material. *Nat. Commun.* **15**, 6727 (2024).
102. Martínez, L. J. et al. Efficient single photon emission from a high-purity hexagonal boron nitride crystal. *Phys. Rev. B* **94**, 121405 (2016).
103. Stern, H. L. et al. Spectrally resolved photodynamics of individual emitters in large-area monolayers of hexagonal boron nitride. *ACS Nano* **13**, 4538–4547 (2019).
104. Tran, T. T., Bray, K., Ford, M. J., Toth, M. & Aharonovich, I. Quantum emission from hexagonal boron nitride monolayers. *Nat. Nanotechnol.* **11**, 37–41 (2016).
105. Fataftah, M. S. & Freedman, D. E. Progress towards creating optically addressable molecular qubits. *Chem. Commun.* **54**, 13773–13781 (2018).
106. Atzori, M. & Sessoli, R. The second quantum revolution: role and challenges of molecular chemistry. *J. Am. Chem. Soc.* **141**, 11339–11352 (2019).
107. Wasielewski, M. R. et al. Exploiting chemistry and molecular systems for quantum information science. *Nat. Rev. Chem.* **4**, 490–504 (2020).
108. Yu, C.-J., von Kugelgen, S., Laorenza, D. W. & Freedman, D. E. A molecular approach to quantum sensing. *ACS Cent. Sci.* **7**, 712–723 (2021).
109. Wasielewski, M. R. Light-driven spin chemistry for quantum information science. *Phys. Today* **76**, 28–34 (2023).
110. Quintes, T., Mayländer, M. & Richert, S. Properties and applications of photoexcited chromophore-radical systems. *Nat. Rev. Chem.* **7**, 75–90 (2023).
111. Bayliss, S. L. et al. Enhancing spin coherence in optically addressable molecular qubits through host-matrix control. *Phys. Rev. X* **12**, 031028 (2022).
112. Breiland, W. G., Brenner, H. C. & Harris, C. B. Coherence in multilevel systems. i. coherence in excited states and its application to optically detected magnetic resonance in phosphorescent triplet states. *J. Chem. Phys.* **62**, 3458–3475 (1975).
113. Hirota, N., Baba, M., Hirata, Y. & Nagaoka, S. Odmr and epr studies of the triplet states of aliphatic and aromatic carbonyls. *J. Phys. Chem.* 83, 3350–3354 (1979).
114. Clarke, R. H. et al. *Triplet State ODMR Spectroscopy: Techniques and Applications to Biophysical Systems* (Wiley, 1982).
115. Kamyshny, A. L., Suisalu, A. P. & Aslanov, L. A. ODMR spectroscopy of coordination compounds. *Coord. Chem. Rev.* **117**, 1–43 (1992).

116. Gückel, F. et al. Odmr of triplet states of cofacial dimeric zinc porphyrins. *Chem. Phys.* **86**, 161–172 (1984).
117. Schaafsma, T., Dag, I., Sitters, R., Glasbeek, M. & Lifshitz, E. Spectroscopy and photophysics of self-organized zinc porphyrin nanolayers. 3. fluorescence detected magnetic resonance of triplet states. *J. Phys. Chem. B* **109**, 17047–17054 (2005).
118. Wrachtrup, J., von Borczyskowski, C., Bernard, J., Orrit, M. & Brown, R. Optically detected spin coherence of single molecules. *Phys. Rev. Lett.* **71**, 3565–3568 (1993).
119. Wrachtrup, J., von Borczyskowski, C., Bernard, J., Orrit, M. & Brown, R. Optical detection of magnetic resonance in a single molecule. *Nature* **363**, 244–245 (1993).
120. Fluorescence-detected coherent phenomena on single triplet-state molecules. In *11th International Vavilov Conference on Nonlinear Optics* vol. **3485**, 98. http://spiedl.org/terms (1998).
121. Singh, H. et al. Room-temperature quantum sensing with photoexcited triplet electrons in organic crystals. *Phys. Rev. Res.* **7**, 013192 (2025).
122. Singh, H. et al. High sensitivity pressure and temperature quantum sensing in pentacene-doped p-terphenyl single crystals. *Nat. Commun.* **16**, 10530 (2025).
123. Mena, A. et al. Room-Temperature Optically Detected Coherent Control of Molecular Spins. *Phys. Rev. Lett.* **133**, 120801 (2024).
124. Ishiwata, H., Song, J., Shigeno, Y., Nishimura, K. & Yanai, N. Molecular quantum nanosensors functioning in living cells. *ChemRxiv* https://doi.org/10.26434/chemrxiv-2025-v0k8g (2025).
125. Ng, W. et al. Move aside pentacene: diazapentacene doped para terphenyl, a zero field room temperature maser with strong coupling for cavity quantum electrodynamics. *Adv. Mater.* **35**, 2300441 (2023).
126. Mann, S. K. et al. Chemically tuning room temperature pulsed optically detected magnetic resonance. *J. Am. Chem. Soc*. https://doi.org/10.1021/jacs.5c05505 (2025).
127. Moro, F. et al. Room-temperature optically detected magnetic resonance of triplet excitons in a pentacene-doped picene single crystal. *J. Mater. Res.* **37**, 1269–1279 (2022).
128. Clarke, R. H. & Frank, H. A. Triplet state radiationless transitions in polycyclic hydrocarbons. *J. Chem. Phys.* **65**, 39–47 (1976).
129. Bräuchle, C., Kabza, H. & Voitländer, J. Optical and odmr investigations of the lowest excited triplet state of dinaphtho-(2'.3':1.2); (2".3":6.7)-pyrene. *Z. Naturforsch.* **34a**, 6–12 (1979).
130. Agostini, G., Corvaja, C., Giacometti, G. & Pasimeni, L. Optical, zero-field ODMR and EPR studies of the triplet states from singlet fission in biphenyl-tcnq and biphenyl-tetrafluoro-tcnq charge-transfer crystals. *Chem. Phys.* **173**, 177–186 (1993).
131. Gundel, D. et al. A quasi-neutral triplet state of tcnq in phenazine/tcnq and fluorene/tcnq ct crystals. *Chem. Phys.* **132**, 363–372 (1989).
132. Corvaja, C., Franco, L., Salikhov, K. M. & Voronkova, V. K. The first observation of electron spin polarization in the excited triplet states caused by the triplet-triplet annihilation. *Appl. Magn. Reson.* **28**, 181–193 (2005).
133. Corvaja, C., Franco, L., Pasimeni, L. & Toffoletti, A. Time resolved EPR of triplet excitons in phenazine-tcnq charge transfer crystal. *Appl. Magn. Reson.* **3**, 797–813 (1992).
134. Gorgon, S. et al. Reversible spin-optical interface in luminescent organic radicals. *Nature* **620**, 538–544 (2023).
135. Chowdhury, R. et al. Bright triplet and bright charge-separated singlet excitons in organic diradicals enable optical read-out and writing of spin states. *Nat. Chem.* **17**, 1410–1417 (2025).
136. Kopp, S. M. et al. Optically detected coherent spin control of organic molecular color center qubits. *J. Am. Chem. Soc.* https://doi.org/10.1021/jacs.5c05718 (2025).
137. Joshi, G. et al. Optical readout of singlet fission biexcitons in a heteroacene with photoluminescence detected magnetic resonance. *J. Chem. Phys.* **157**, 164702 (2022).
138. Sun, Y. et al. SSpin-dependent recombination mechanisms for quintet biexcitons generated through singlet fission. *Phys. Rev. B* **108**, 184203 (2023).
139. Grüne, J. et al. High-spin state dynamics and quintet-mediated emission in intramolecular singlet fission. *arXiv* http://arxiv.org/abs/2410.07891 (2024).
140. Zhu, Y., Zhu, Z., Wang, S., Peng, Q. & Abdurahman, A. Stable luminescent diradicals: the emergence and potential applications. *Angew. Chem. Int. Ed*. **64**,https://onlinelibrary.wiley.com/doi/10.1002/anie.202423470 (2025).
141. Samal, S. et al. Physical, thermal, and mechanical characterization of PMMA foils fabricated by solution casting. *Appl. Sci.* **13**, 6445 (2023).
142. Kwiram, A. L. & Ross, J. B. A. Optical detection of magnetic resonance in biologically important molecules. *Annu. Rev. Biophys. Bioeng.* **11**, 223–249 (1982).
143. Feder, J. S. et al. A fluorescent-protein spin qubit. *Nature* **645**, 73–79 (2025).
144. Braun, D., Schweitzer, D. & Yersin, H. Zero-field splitting of the lowest excited state of tris(bipyridine)osmium(2+) doped into tris(bipyridine)ruthenium(ii) bis(hexafluorophosphate). *J. Phys. Chem.* **93**, 7555–7556 (1989).
145. Weissbart & Brian. Optical and ODMR spectroscopy: studies of closed shell metal complexes. PhD thesis, Univ. California, Davis (1994).
146. Westra, J. & Glasbeek, M. Spin dynamics in the photo-excited triplet state of Rh^{3+}-trisbipyridyl perchlorate. *Chem. Phys. Lett.* **180**, 41–44 (1991).
147. Glasbeek, M. Excited state spectroscopy and excited state dynamics of Rh(III) and Pd(II) chelates as studied by optically detected magnetic resonance techniques. In *Transition Metal Complexes: Dynamics and Reactivity* vol. **I**, 95–142 (Springer, 2001).
148. Fields, R., Winscom, C., Haindl, E., Plato, M. & Möbius, K. Optically detected magnetic resonance (odmr) of the lowest doublet excited state of tris(acetylacetonato)chromium(iii). *Chem. Phys. Lett.* **124**, 121–127 (1986).
149. Geschwind, S., Devlin, G. E., Cohen, R. L. & Chinn, S. R. Orbach relaxation and hyperfine structure in the excited $E(^2E)$ state of Cr^{3+} in Al_2O_3. *Phys. Rev.* **137**, A1087 (1965).
150. Laorenza, D. W. et al. Tunable Cr^{4+} molecular color centers. *J. Am. Chem. Soc.* **143**, 21350–21363 (2021).
151. Bayliss, S. L. et al. Optically addressable molecular spins for quantum information processing. *Science* **370**, 1309–1312 (2020).
152. Bayliss, S. L. et al. Enhancing spin coherence in optically addressable molecular qubits through host-matrix control. *Phys. Rev. X* **12**, 31028 (2022).
153. Wojnar, M. K., Laorenza, D. W., Schaller, R. D. & Freedman, D. E. Nickel(II) metal complexes as optically addressable qubit candidates. *J. Am. Chem. Soc.* **142**, 14826–14830 (2020).
154. Wojnar, M. K. et al. Ligand field design enables quantum manipulation of spins in Ni^{2+} complexes. *Chem. Sci.* **15**, 1374–1383 (2024).
155. Laorenza, D. W. et al. Coherent spin-control of s = 1 vanadium and molybdenum complexes. *Chem. Sci.* **15**, 14016–14026 (2024).
156. Fataftah, M. S. et al. Trigonal sipyramidal V^{3+} complex as an optically addressable molecular qubit candidate. *J. Am. Chem. Soc.* **142**, 20400–20408 (2020).
157. Bruzewicz, C. D., Chiaverini, J., McConnell, R. & Sage, J. M. Trapped-ion quantum computing: progress and challenges. *Appl. Phys. Rev.* **6**, 021314 (2019).
158. Brown, K. R., Chiaverini, J., Sage, J. M. & Häffner, H. Materials challenges for trapped-ion quantum computers. *Nat. Rev. Mater.* **6**, 892–905 (2021).
159. Moses, S. A. et al. A race-track trapped-ion quantum processor. *Phys. Rev. X* **13**, 041052 (2023).

160. Sorace, L. et al. *Lanthanides and Actinides in Molecular Magnetism* (Wiley, 2015). https://onlinelibrary.wiley.com/doi/book/10.1002/9783527673476.
161. iang, S.-D., Wang, B.-W. & Gao, S. Advances in lanthanide single-ion magnets. In *Structure and Bonding* vol. **164**, 111–141 (Springer Nature, 2014)
162. Parker, D., Suturina, E. A., Kuprov, I. & Chilton, N. F. How the ligand field in lanthanide coordination complexes determines magnetic susceptibility anisotropy, paramagnetic NMR shift, and relaxation behavior. *Acc. Chem. Res.* **53**, 1520–1534 (2020).
163. Gaita-Ariño, A., Luis, F., Hill, S. & Coronado, E. Molecular spins for quantum computation. *Nat. Chem.* **11**, 301–309 (2019).
164. Aromí, G. & Roubeau, O. Lanthanide molecules for spin-based quantum technologies. In *Handbook on the Physics and Chemistry of Rare Earths* vol. **56**, 1–54 (Elsevier, 2019).
165. Liang, P. et al. Room-temperature electron spin dynamics of Ce^{3+} ions in a YAG crystal. *Appl. Phys. Lett.* **110**, 3–8 (2017).
166. Yano, R., Mitsunaga, M. & Uesugi, N. Ultralong optical dephasing time in Eu^{3+}:Y_2SiO_5. *Opt. Lett.* **16**, 1884 (1991).
167. Equall, R. W., Cone, R. L. & Macfarlane, R. M. Homogeneous broadening and hyperfine structure of optical transitions in Pr^{3+}:Y_2SiO_5. *Phys. Rev. B* **52**, 3963–3969 (1995).
168. Ortu, A. et al. Simultaneous coherence enhancement of optical and microwave transitions in solid-state electronic spins. *Nat. Mater.* **17**, 671–675 (2018).
169. Jobbitt, N. L., Wells, J.-P. R., Reid, M. F. & Longdell, J. J. Raman heterodyne determination of the magnetic anisotropy for the ground and optically excited states of Y_2SiO_5 doped with Sm^{3+}. *Phys. Rev. B* **103**, 205114 (2021).
170. Shoudu, Z. et al. Czochralski growth of rare-earth orthosilicates-Y_2SiO_5 single crystals. *J. Cryst. Growth* **197**, 901–904 (1999).
171. Fraval, E., Sellars, M. J. & Longdell, J. J. Method of extending hyperfine coherence times in Pr^{3+}:Y_2SiO_5. *Phys. Rev. Lett.* **92**, 077601 (2004).
172. Fraval, E., Sellars, M. J. & Longdell, J. J. Dynamic decoherence control of a solid-state nuclear-quadrupole qubit. *Phys. Rev. Lett.* **95**, 8–11 (2005).
173. Zhong, M., Ahlefeldt, R. L. & Sellars, M. J. Quantum information processing using frozen core Y^{3+} spins in Eu^{3+}:Y_2SiO_5. *N. J. Phys.* **21**, 033019 (2019).
174. McAuslan, D. L., Bartholomew, J. G., Sellars, M. J. & Longdell, J. J. Reducing decoherence in optical and spin transitions in rare-earth-metal-ion-doped materials. *Phys. Rev. A* **85**, 032339 (2012).
175. Zhong, M. et al. Optically addressable nuclear spins in a solid with a six-hour coherence time. *Nature* **517**, 177–180 (2015).
176. Heinze, G., Hubrich, C. & Halfmann, T. Hyperfine characterization and spin coherence lifetime extension in Pr^{3+}:$La_2(WO_4)_3$. *Phys. Rev. A* **89**, 053825 (2014).
177. Lovrić, M. et al. Hyperfine characterization and spin coherence lifetime extension in Pr^{3+}:$La_2(WO_4)_3$. *Phys. Rev. B* **84**, 104417 (2011).
178. Böttger, T., Harris, T. L., Reinemer, G. D., Thiel, C. W. & Cone, R. L. Optical decoherence, spectroscopy, and magnetic g tensors for the 1.5-um $^4I_{15/2}$ - $^4I_{13/2}$ transitions of Er^{3+} dopants at the C_2-symmetry site in Y_2O_3. *Phys. Rev. B* **110**, 045132 (2024).
179. Böttger, T., Thiel, C., Sun, Y., Macfarlane, R. & Cone, R. Decoherence and absorption of Er^{3+}:$KTiOPO_4$ (KTP) at 1.5 μm. *J. Lumin.* **169**, 466–471 (2016).
180. Böttger, T., Thiel, C. W., Cone, R. L., Sun, Y. & Faraon, A. Optical spectroscopy and decoherence studies of Yb^{3+}:YAG at 968 nm. *Phys. Rev. B* **94**, 045134 (2016).
181. Lim, H.-J., Welinski, S., Ferrier, A., Goldner, P. & Morton, J. J. L. Coherent spin dynamics of ytterbium ions in yttrium orthosilicate. *Phys. Rev. B* **97**, 064409 (2018).
182. Welinski, S. et al. Coherence time extension by large-scale optical spin polarization in a rare-earth doped crystal. *Phys. Rev. X* **10**, 031060 (2020).
183. Jobbitt, N. L., Wells, J.-P. R. & Reid, M. F. Zeeman and laser site selective spectroscopy of C 1 point group symmetry Sm^{3+} centres in Y_2SiO_5: a parametrized crystal-field analysis for the 4f 5 configuration. *J. Phys.: Condens. Matter* **34**, 325502 (2022).
184. Kolesov, R. et al. Mapping spin coherence of a single rare-earth ion in a crystal onto a single photon polarization state. *Phys. Rev. Lett.* **111**, 120502 (2013).
185. Xia, K. et al. All-optical preparation of coherent dark states of a single rare earth ion spin in a crystal. *Phys. Rev. Lett.* **115**, 093602 (2015).
186. Belykh, V. V. & Melyakov, S. R. Selective measurement of the longitudinal electron spin relaxation time T_1 of Ce^{3+} ions in a YAG lattice: resonant spin inertia. *Phys. Rev. B* **105**, 205129 (2022).
187. Azamat, D. V. et al. Electron spin dynamics of Ce^{3+} ions in YAG crystals studied by pulse-EPR and pump-probe Faraday rotation. *Phys. Rev. B* **96**, 075160 (2017).
188. Tolmachev, D. O. et al. Paramagnetic Ce^{3+} optical emitters in garnets: optically detected magnetic resonance study and evidence of Gd-Ce cross-relaxation effects. *Phys. Rev. B* **95**, 224414 (2017).
189. Edinach, E. V. et al. Electronic structure of non-Kramers Tb^{3+} centers in garnet crystals and evidence of their energy and spin transfer to Ce^{3+} emitters. *Phys. Rev. B* **100**, 104435 (2019).
190. Chai, Z. et al. Coherence properties of rare-earth spins in micrometer-thin films. *ACS Photonics* **12**, 2515–2521 (2025).
191. Zhang, X. & Hu, E. L. Templated growth of diamond optical resonators via plasma-enhanced chemical vapor deposition. *Appl. Phys. Lett.* **109**, 081110 (2016).
192. Chen, Y.-C. et al. Laser writing of coherent colour centres in diamond. *Nat. Photonics* **11**, 77–80 (2016).
193. Roggors, S. et al. Optically detected magnetic resonance on carbene molecular qubits. *J. Am. Chem. Soc.* **147**, 36383–36392 (2025).
194. Liu, G.-Q., Feng, X., Wang, N., Li, Q. & Liu, R.-B. Coherent quantum control of nitrogen-vacancy center spins near 1000 kelvin. *Nat. Commun.* **10**, 1344 (2019).
195. Engels, J. et al. High ODMR contrast and alignment of NV centers in microstructures grown on heteroepitaxial diamonds. *Appl. Phys. Lett.* **124**, 164001 (2024).
196. Sukachev, D. D. et al. Silicon-vacancy spin qubit in diamond: a quantum memory exceeding 10 ms with single-shot state readout. *Phys. Rev. Lett.* **119**, 223602 (2017).
197. Crook, A. L. et al. Purcell enhancement of a single silicon carbide color center with coherent spin control. *Nano Lett.* **20**, 3427–3434 (2020).
198. Li, Q. et al. Room-temperature coherent manipulation of single-spin qubits in silicon carbide with a high readout contrast. *Natl. Sci. Rev.* **9**, nwab122 (2022).
199. Lin, W.-X. et al. Temperature dependence of divacancy spin coherence in implanted silicon carbide. *Phys. Rev. B* **104**, 125305 (2021).
200. Dieke, G. H. *Spectra and Energy Levels of Rare Earth Ions in Crystals* (John Wiley and Sons, 1968).
201. Thiel, C. et al. Optical decoherence and persistent spectral hole burning in Er^{3+}:$LiNbO_3$. *J. Lumin.* **130**, 1603–1609 (2010).
202. Belykh, V., Korotneva, A. & Yakovlev, D. Stimulated resonant spin amplification reveals millisecond electron spin coherence time of rare-earth ions in solids. *Phys. Rev. Lett.* **127**, 157401 (2021).
203. Dargyte, U., Lancaster, D. M. & Weinstein, J. D. Optical and spin-coherence properties of rubidium atoms trapped in solid neon. *Phys. Rev. A* **104**, 032611 (2021).
204. Bergeron, L. et al. Silicon-integrated telecommunications photon-spin interface. *PRX Quantum* **1**, 020301 (2020).

205. Glasbeek, M. & Hond, R. Phase relaxation of photoexcited triplet spins in CaO. *Phys. Rev. B* **23**, 4220–4235 (1981).
206. Müller, T. et al. Optical signatures of silicon-vacancy spins in diamond. *Nat. Commun.* **5**, 3328 (2014).
207. Davidsson, J. et al. First principles predictions of magneto-optical data for semiconductor point defect identification: the case of divacancy defects in 4H-SiC. *N. J. Phys.* **20**, 023035 (2018).
208. Bathen, M. E. & Vines, L. Manipulating single photon emission from point defects in diamond and silicon carbide. *Adv. Quantum Technol.* **4**, 1–19 (2021).
209. Wolfowicz, G. et al. Optical charge state control of spin defects in 4H-SiC. *Nat. Commun.* **8**, 2–10 (2017).
210. Cui, S. et al. Growth regulation of pentacene-doped p-terphenyl crystals on their physical properties for promising maser gain medium. *Cryst. Growth Des.* **20**, 783–792 (2020).
211. Longdell, J. J., Alexander, A. L. & Sellars, M. J. Characterization of the hyperfine interaction in europium-doped yttrium orthosilicate and europium chloride hexahydrate. *Phys. Rev. B Condens. Matter Mater. Phys.* **74**, 1–7 (2006).
212. Böttger, T., Sun, Y., Thiel, C. W. & Cone, R. L. Spectroscopy and dynamics of Er^{3+}:Y_2SiO_5 at 1.5 μm. *Phys. Rev. B* **74**, 075107 (2006).

Acknowledgements

This work was supported by the UK Engineering and Physical Science Research Council through grants EP/V048430/1 and EP/W027542/1, and the Department of Materials, Imperial College London. The authors are also very grateful to Dr Daan M. Arroo for fruitful discussions and advice.

Author contributions

C.A.T. and M.A. curated the data. C.A.T., M.O., and M.A. contributed to the writing of the manuscript. All authors have read and approved the manuscript.

Competing interests

The authors declare no competing interests.

Additional information

Supplementary information The online version contains supplementary material available at https://doi.org/10.1038/s41535-026-00877-5.

Correspondence and requests for materials should be addressed to Mark Oxborrow or Max Attwood.

Reprints and permissions information is available at http://www.nature.com/reprints

Publisher's note Springer Nature remains neutral with regard to jurisdictional claims in published maps and institutional affiliations.

Open Access This article is licensed under a Creative Commons Attribution 4.0 International License, which permits use, sharing, adaptation, distribution and reproduction in any medium or format, as long as you give appropriate credit to the original author(s) and the source, provide a link to the Creative Commons licence, and indicate if changes were made. The images or other third party material in this article are included in the article's Creative Commons licence, unless indicated otherwise in a credit line to the material. If material is not included in the article's Creative Commons licence and your intended use is not permitted by statutory regulation or exceeds the permitted use, you will need to obtain permission directly from the copyright holder. To view a copy of this licence, visit http://creativecommons.org/licenses/by/4.0/.

© The Author(s) 2026